# Some mathematical problems associated with the development and use of marine models

Eric DELEERSNIJDER*, Jean-Marie BECKERS**, Jean-Michel CAMPIN, Mohammed EL MOHAJIR, Thierry FICHEFET* and Patrick LUYTEN***

Institut d'Astronomie et de Géophysique G. Lemaître
Université Catholique de Louvain
2 Chemin du Cyclotron, B-1348 Louvain-la-Neuve, Belgium



## 1. Introduction

"Science is now a tripartite endeavour with *simulation* added to the two classical components, *experiment* and *theory* (Robinson, 1987). The routine use of numerical "simulation in scientific research (numerical experimentation, sensitivity and process studies, etc.) is thought by many to represent the first major step forward in the basic scientific method since the seventeenth century" (Robinson, 1987).

Marine sciences, as many other fields of scientific research, now intensively use mathematical and numerical models. There might even be a tendency, among some oceanographers, to overly rely on the predictions of the models, which are, in fact, no more than artefacts, *i.e.*, man-made objects. The models, however complex they may be, provide, at best, a reasonable estimate of the behaviour of the system under study.

Numerical models are now so appealing that one might progressively forget that they are no substitute to reality. To avoid such "alienation", it is helpful to realized that there are several types of models, with different objectives. According to Nihoul (1994) one may distinguish:

— The *test-oriented models*, which are needed for "testing mathematical and numerical methods and their software implementation". These models are based on a reduced set of equations and, hence, are generally not intended to realistically simulate the reality.

— The *process-oriented models*, which focus on a few dominant or important processes. This often implies sacrificing some of the realism of the results, but allows detailed analysis of the mechanisms driving the system under study to be carried out.

— The *system-oriented models*, which are "called upon to tackle a practical situation", such as the management of the resources of the seas. The results of these models must be as realistic as possible, which usually requires appropriate data assimilation procedure to operate together with the prognostic model (Bennett, 1992). Encompassing a large number of processes, system-oriented models are generally very complex, so that they are probably not the best suited tool for investigating or "explaining" processes.

---

* *Research Associate, National Fund for Scientific Research (Belgium)*
** *Senior Research Assistant, National Fund for Scientific Research (Belgium); GHER, University of Liège, Sart Tilman B5, B-4000 Liège, Belgium*
*** *MUMM, Gulledelle 100, B-1200 Brussels, Belgium*

NATO ASI Series, Vol. I 48
The Mathematics of Models for Climatology and Environment
Edited by Jesús Ildefonso Díaz

Working out a system-oriented model, as well as interpreting its results, generally poses several mathematical problems, which may sometimes be addressed with the help of simpler, test-oriented models. Some of these problems are considered below.

For example, the numerical scheme selected for solving the equations of the model must provide accurate results. To do so, the algorithm must be, at least, consistent and stable. In most cases, consistency is easily checked. On the other hand, verifying that the numerical scheme associated with a system-oriented model is stable often presents insurmountable difficulties, for the equations are very complex. The usual approach is then to analyse sub-sets of the whole algorithm, especially those that are likely to be the least stable. Properly choosing the reduced sets of equations is thus the key problem. Any inappropriate choice may give rise to unpleasant surprises, as exemplified in Section 3 (see also Beckers and Deleersnijder, 1993).

Another significant problem is the well-foundedness of the parameterizations. No numerical model is able to cover all the time-space scales of marine phenomena. Once the resolution of the model is chosen, the effect of the processes having smaller scales than the time-space discretization grid, the so-called sub-grid scale phenomena, must be parameterized by appropriate formulae. A parameterization is merely an approximation, hopefully providing a reasonably good account of the process it addresses. It is thus conceivable that, for a given sub-grid scale phenomenon, several parameterizations may be considered. The formulation to be selected must obviously be capable of realistically representing the effect it addresses. More importantly, perhaps, it must also be well-conditioned, *i.e.*, when introduced into the model, it must enable the model to produce well-behaved solutions. The latter property does not necessarily ensue from the parameterization being sufficiently realistic, as will be shown in Section 4 (see also Deleersnijder and Luyten, 1994).

Complex marine models routinely output millions, or even billions, of real numbers, the analysis and interpretation of which are far from straightforward. In fact, understanding such a large amount of information is a real challenge. Simple models may be helpful for interpreting the results of a complex one. Most quantities computed by marine models are four-dimensional, *i.e.*, they depend on time and three space coordinates. Since the vast majority of the graphical tools are two- or three-dimensional, the graphical representation of the model results requires appropriate mapping onto a two- or three-dimensional space. This may be carried out in numerous ways by means of existing graphical packages. One must however bear in mind that the role of computer graphics is not just to produce attractive pictures, but to help gain insight into the physics of the marine flow under study. In other words, physical intuition and reasoning are also needed if profound understanding of the flow mechanisms is sought. Schematically, this may be expressed by the following relation: quality of the interpretation = (physical skill) x (computer graphics skill). This implies, for instance, that the best graphical software will probably prove useless if operated by someone having no idea of ocean dynamics! An example of an interpretation method based on little graphical skill but considerable physical skill is given in Section 5, where the vertical velocity field produced by a hydrodynamic model of the region of the Bering Strait is analyzed (see also Deleersnijder 1994a).

Finally, in Section 6, some results of a World Ocean model are given. Its equations are similar to those used at smaller scales, but the nature of the phenomena is completely different. A coordinate system is designed in such a way that the whole World Ocean, including the Arctic Ocean, can be represented without facing any singularity problem — as would happen,



at the North Pole, with standard spherical coordinates. To avoid dealing with three-dimensional velocity fields, the results are analysed with the help of the so-called meridional stream function technique.

Before examining the specific problems listed above, the equations of marine hydrodynamics are briefly established (Section 2).

## 2. Equations of marine hydrodynamics

The equations governing marine hydrodynamics processes are derived from the general theory of fluid mechanics.

Reynolds (1883) realized that there are two types of fluid flow, the laminar mode and the turbulent mode, in which apparently erratic fluctuations occur. Reynolds (1894) suggested filtering out the fluctuations and concentrating on the "mean" flow, considered as a laminar one with modified properties and equations.

Reynolds mostly studied flows he could produce in his laboratory, *i.e.*, small-scale flows. In the ocean, however, analogous turbulent processes may be found in the surface and bottom boundary layers, the thickness of which is of order 10-100 m for the former, and 1-10 m for the latter. The interior of the ocean experiences intermittent turbulence: at any instant, the total volume of the turbulent spots does not exceed a few percents of the whole ocean volume.

Over the continental shelves, the seas are so shallow — with depth of order 10-100 m —, and the processes generating turbulence may be so intense, that the surface and bottom boundary layers may merge, resulting in a wholly turbulent water column.

The time scales of marine turbulence range from seconds to minutes, while the length scales are of order $10^{-3}$-$10^{0}$ m.

Most marine models, whether designed for deep or shallow sea problems, do not resolve the turbulent scales of motion, implying that the turbulent processes appear as sub-grid scale effects to be parameterized. Let $\mathbf{v}'$ and $c'$ denote the turbulent part of the velocity $\mathbf{v}^*$ and of any scalar quantity $c^*$, of which the mean parts read $\mathbf{v}$ and $c$, respectively. Thus, $\mathbf{v}^* = \mathbf{v} + \mathbf{v}'$ and $c^* = c + c'$. The mean — or filtered — variables $\mathbf{v}$ and $c$ are part of the prognostic quantities of the model, *i.e.*, there exist equations for the time derivatives of $\mathbf{v}$ and $c$, obtained by averaging the basic governing equations — which are, in principle, capable of resolving the turbulent scales.

For simplicity, it is hypothesized that the averaging operator — hereafter denoted "$\langle\ \rangle$" — enjoys all the simplest properties of every sensible averaging operator one might consider (for a review, see Bedford *et al.*, 1987).

As is usual in marine modelling, the Boussinesq approximation is assumed valid, so that the density variations are neglected, except in the gravitational force. Accordingly, the average of the advection terms of the governing equations reads

$$\Diamond\bullet\langle \mathbf{v}^* \mathbf{v}^* \rangle = \Diamond\bullet(\mathbf{v}\,\mathbf{v}) + \Diamond\bullet\langle \mathbf{v}'\,\mathbf{v}' \rangle \,, \tag{1}$$

$$\Diamond\bullet\langle \mathbf{v}^* c^* \rangle = \Diamond\bullet(\mathbf{v}\,c) + \Diamond\bullet\langle \mathbf{v}'\,c' \rangle \,, \tag{2}$$

where "$\Diamond\bullet$" is the divergence operator. The first term in the right-hand side of (1) and (2) only encompasses prognostic variables, rendering its evaluation feasible. By contrast, $\Diamond\bullet\langle \mathbf{v}'\,\mathbf{v}' \rangle$ and $\Diamond\bullet\langle \mathbf{v}'\,c' \rangle$ do not contain prognostic quantities and, in fact, appear as additional unknowns, pointing to the need for appropriate closure assumptions.

As first suggested by Boussinesq (1877), Fourier-Fick-type parameterizations may be resorted to, yielding

$$\langle \mathbf{v}'\mathbf{v}' \rangle = -K_v [\, \Diamond \mathbf{v} + (\Diamond \mathbf{v})^T \,] + (q^2/3)\, \mathbf{I} \,, \tag{3}$$

$$\langle \mathbf{v}' c' \rangle = -K_c \Diamond c \,, \tag{4}$$

where $(\Diamond \mathbf{v})^T$ is the transposed of the tensor $\Diamond \mathbf{v}$; $\mathbf{I}$ is the identity tensor; $q^2/2 = \langle \mathbf{v}' \bullet \mathbf{v}' \rangle$ denotes the turbulent kinetic energy; $K_v$ and $K_c$ represent the turbulent, or "eddy", viscosity and diffusivity, respectively. The latter are generally of order $10^{-1}$-$10^{-4}$ m$^2$ s$^{-1}$, *i.e.*, several orders of magnitude larger than their molecular counterparts, which are $\lesssim 10^{-6}$ m$^2$ s$^{-1}$.

The depth of marine computational domains is, in most cases, much smaller that the horizontal extent, for the processes under study have a small aspect ratio — which is defined as the ratio of the vertical length scale to the horizontal one. As a result, the divergence of the turbulent flux of $c$ may be approximated by

$$\Diamond \bullet \langle \mathbf{v}' c' \rangle \sim \frac{\partial \langle w' c' \rangle}{\partial z} = \frac{\partial}{\partial z}\left(-K_c \frac{\partial c}{\partial z}\right) \,, \tag{5}$$

where $z$ and $w$ are the vertical coordinate and the vertical velocity, respectively.

The hydrostatic approximation is assumed valid, in agreement with the aspect ratio being small. Therefore, we only need to examine the turbulent flux of horizontal momentum, $\langle \mathbf{v}' \mathbf{u}' \rangle$, where $\mathbf{u}'$ denotes the fluctuating horizontal velocity. Because of the smallness of the aspect ratio, $\Diamond \bullet \langle \mathbf{v}' \mathbf{u}' \rangle$ may be reduced to

$$\Diamond \bullet \langle \mathbf{v}' \mathbf{u}' \rangle \sim \frac{\partial \langle w' \mathbf{u}' \rangle}{\partial z} = \frac{\partial}{\partial z}\left(-K_u \frac{\partial \mathbf{u}}{\partial z}\right) \,. \tag{6}$$

We are thus left with the problem of computing the eddy viscosity $K_u$ and the eddy diffusivity $K_c$. To do so, many turbulence closure models have been suggested in the literature (for a review, see Mellor and Yamada (1982), Rodi (1993) or Luyten *et al.* (1994)).

According to the discussion above, the generic form of the governing equations of marine hydrodynamics reads

$$\frac{\partial \psi}{\partial t} + \nabla \bullet (\mathbf{u}\psi) + \frac{\partial (w\,\psi)}{\partial z} = Q^\psi + \nabla \bullet (A_\psi \nabla \psi) + \frac{\partial}{\partial z}\left(K_\psi \frac{\partial \psi}{\partial z}\right) \,, \tag{7}$$

where $\psi$ is a given prognostic variable (see Table 1); $\mathbf{u}$ and $w$ denote the horizontal velocity vector and the vertical velocity, respectively; $t$ represents time while $\nabla$ is the horizontal "gradient operator", *i.e.*, $\nabla = \mathbf{e}_x \partial/\partial x + \mathbf{e}_y \partial/\partial y$ ($\mathbf{e}_x$ and $\mathbf{e}_y$ being the horizontal unit vectors associated with the horizontal coordinates, $x$ and $y$); $Q^\psi$ is an appropriate source/sink term. At this stage, it is sufficient to use cartesian coordinates, but the equations may be re-formulated in another coordinate system according to the type of problem considered (see Sections 5 and 6).

The horizontal diffusivity $A_\psi$ is not associated with "proper" three-dimensional turbulent phenomena. The horizontal diffusion flux $-A_\psi \nabla \psi$ represents mainly horizontal motions that cannot be resolved by the numerical grid. Moreover, horizontal diffusion is generally needed to filter out small-scale computational noise, arising because of the nonlinearity of the equations. In general, $A_\psi$ depends on the grid size and is much larger than the vertical diffusivity $K_\psi$. Large uncertainties commonly exist as to the determination of $A_\psi$. The horizontal viscosity may



be in the range 1-$10^6$ m$^2$ s$^{-1}$, while the horizontal diffusivity generally is such that $1 \text{ m}^2 \text{ s}^{-1} \lesssim A_c \lesssim 10^4 \text{ m}^2 \text{ s}^{-1}$.

*Table 1.* The values of $\psi$ and $Q^\psi$, in accordance with (7), are given in this table. The Coriolis parameter is denoted $f$ ($\approx \pm 10^{-4}$ s$^{-1}$ at mid latitudes, $= 0$ at the Equator), while $\mathbf{e}_z$, $p$ and $\rho$ represent the vertical unit vector, the pressure and the density, respectively. In the scope of the Boussinesq approximation, $\rho$ is considered equal to an appropriate — constant — reference value $\rho_0$ ($\approx 1025$ kg m$^{-3}$), except in the weight $-\rho g$, where $g$ is the gravitational acceleration ($\approx 9.8$ m$^2$ s$^{-1}$). The variable $c$ represents any scalar quantity, for instance, temperature, salinity, concentration of a pollutant...

| | $\psi$ | $Q^\psi$ |
|---|---|---|
| continuity equation | 1 | 0 |
| horiz. momentum eq. | $\mathbf{u}$ | $-f\mathbf{e}_z \times \mathbf{u} - \rho_0^{-1} \nabla p$ |
| vert. momentum eq. | 0 | $-\rho^{-1} \partial p/\partial z - g$ |
| scalar quantity budget | $c$ | $= 0$ if passive tracer, $\neq 0$ otherwise |

## 3. Numerical stability of inertia-gravity waves

Large scale atmospheric and oceanic motions roughly obey the geostrophic equilibrium. When imbalances occur, the geostrophic balance is restored by means of inertia-gravity waves (Blumen, 1972). The dynamics of tides and storm surges is dominated by the propagation of external inertia-gravity waves, which are related to the motion of the sea surface. In strongly stratified seas, one also considers the displacement of density surfaces, which leads to internal inertia-gravity waves. The propagation of inertia-gravity waves, be they external or internal, is thus a central issue to many geophysical fluid problems.

The phase speed of external inertia-gravity waves is of order 100 m s$^{-1}$ in the ocean. Internal waves propagate at a few meter per second. Thus, inertia-gravity waves are faster than advective processes, of which the characteristic velocity scale does not exceed 1 m s$^{-1}$. Consequently, inertia-gravity waves are likely to lead to more severe limitation of the time increment of the numerical schemes than the advective phenomena.

There are thus physical and numerical reasons for requiring a careful design of the part of the scheme corresponding to the inertia-gravity waves.

The external linear inertia-gravity waves, also called Poincaré waves, are governed by the following dimensionless equations:

$$\frac{\partial \eta}{\partial t} = -\frac{\partial u}{\partial x} - \frac{\partial v}{\partial y} \,, \tag{8}$$

$$\frac{\partial u}{\partial t} = \gamma v - \frac{\partial \eta}{\partial x} \,, \tag{9}$$

$$\frac{\partial v}{\partial t} = -\gamma u - \frac{\partial \eta}{\partial y} , \qquad (10)$$

where $u$ and $v$ denote horizontal velocity components in the $x$ and $y$ direction, respectively; $\eta$ represents the sea surface elevation. The characteristic length, $L$, and time, $T$, used in the derivation of the dimensionless variables obey $L^2 = ghT^2$, where $h$ is the unperturbed depth of the sea, assumed to be constant. The velocity scale, $U$, and the elevation scale, $E$, satisfy $E^2 = hU^2/g$. In addition, $\gamma$ is defined to be $\gamma = fT$, so that the pure gravity waves correspond to $\gamma = 0$.

The governing equations of internal inertia-gravity waves are similar to (8)-(10), except that $h$, $u$, $v$ and $\eta$ are to be interpreted as equivalent quantities related to the particular internal mode considered (LeBlond and Mysak, 1978).

Various studies focused on the space differencing aspects of (8)-(10). When time differencing is also considered, it is customary to restrict the analysis to pure gravity waves ($\gamma = 0$), for which stability conditions are readily obtained. It is common to content oneself with the latter conditions. Here, a simple space-time differencing scheme is considered. It is seen that the stability condition for the inertia-gravity waves ($\gamma \neq 0$) is far more constraining than that for the pure gravity waves. Indeed, the limit as $\gamma \to 0$ of the stability condition is not equal to the stability condition when $\gamma = 0$.

**Finite-difference schemes.** The four classical space arrangements of the unknowns ($\eta, u, v$) are taken into account, namely the A, B, C and D grids (Fig. 1) — according to Arakawa's classification (Arakawa and Lamb, 1977). The C grid is used in most shallow sea models (*e.g.* Blumberg and Mellor, 1987), while the B-grid is that of the now classical ocean model of Bryan (1969) and Cox (1984). The B grid is believed to be better suited for large scale, low resolution models (Mesinger and Arakawa, 1976), but is also thought to be more prone to numerical noise (Batteen and Han, 1981; Deleersnijder and Campin, 1994).

Centered space differencing is used, as in Arakawa and Lamb (1977). A forward-backward time stepping is selected (Mesinger and Arakawa, 1976). The Coriolis force is prevented from generating — or dissipating — mechanical energy by a simple technique originating from Sielecki (1968) and adapted to ensure symmetry in the $x$ and $y$ directions. Accordingly, the discrete counterparts of (8)-(10) read

$$\eta^{n+1} = \eta^n - \Delta t \, ( d_x u^n + d_y v^n ) , \qquad (11)$$

$$u^{n+1} = u^n - \Delta t \, [ - \gamma s \, \overline{v}^{n+1} - \gamma (1 - s) \, \overline{v}^n + d_x \eta^{n+1} ] , \qquad (12)$$

$$v^{n+1} = v^n - \Delta t \, [ \gamma s \, \overline{u}^n + \gamma (1 - s) \, \overline{u}^{n+1} + d_y \eta^{n+1} ] , \qquad (13)$$

where $n$ is the index associated with the time discretization; $\Delta t$ represents the dimensionless time increment; $s$ is 0 or 1 according to whether $n$ is even or odd; $d_x$ and $d_y$ denote the discrete space derivation operators along the $x$ and $y$ axis, respectively; the overbar refers to the space average that may be needed to evaluate $v$ (or $u$) at a grid node where $u$ (or $v$) is defined.

For instance, the explicit discretized form of continuity equation (11) is expressed as (Fig. 1)



$$\eta^{n+1}_{i,j} = \eta^n_{i,j} - \Delta t \left( \frac{u^n_{i+1/2,j+1/2} + u^n_{i+1/2,j-1/2} - u^n_{i-1/2,j+1/2} - u^n_{i-1/2,j-1/2}}{2\,\Delta x} + \frac{v^n_{i+1/2,j+1/2} + v^n_{i-1/2,j+1/2} - v^n_{i+1/2,j-1/2} - v^n_{i-1/2,j-1/2}}{2\,\Delta y} \right) , \qquad (14)$$

$$\eta^{n+1}_{i,j} = \eta^n_{i,j} - \Delta t \left( \frac{u^n_{i+1/2,j} - u^n_{i-1/2,j}}{\Delta x} + \frac{v^n_{i,j+1/2} - v^n_{i,j-1/2}}{\Delta y} \right) , \qquad (15)$$

for the B and C grid, respectively.

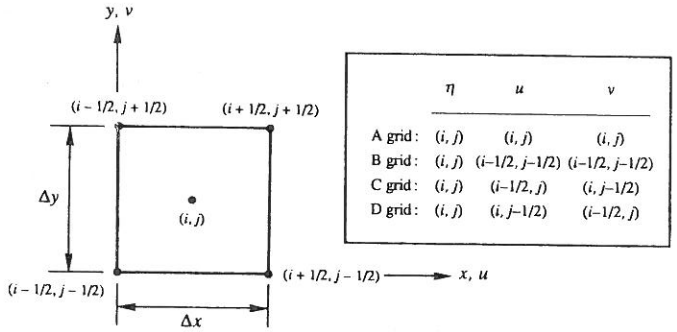


*Figure 1.* Location of the unknowns ($\eta, u, v$) on the A, B, C, and D grids; $i$ and $j$ are integer indices associated with the space discretization. According to the type of grid considered, every variable may be computed at $x = (i - 1/2, i, i + 1/2)\,\Delta x$ and $y = (j - 1/2, j, j + 1/2)\,\Delta y$, where $\Delta x$ and $\Delta y$ denote the space increments.

**Stability analysis.** To perform the von Neumann stability analysis of the above schemes, wave solutions of (11)-(13) are considered in an infinite domain, *i.e.*, every unknown $r$ is assumed to be of the form $r(t, x, y) = R(t) \exp[I\,(k_x x + k_y y)]$, with $I = (-1)^{1/2}$. Wavenumbers $k_x$ and $k_y$ obey the inequalities set out below. A 3x3 amplification matrix is obtained, the eigenvalues, $\lambda$, of which are given by

$$(\lambda - 1)\,(\lambda^2 - 2b\lambda + 1) = 0 . \qquad (16)$$

As the time-independent geostrophic motion is a possible solution to (11)-(13), one eigenvalue must obviously be unity, in accordance with (16). Equations (8)-(10) contain no phenomenon growing in time. Hence, numerical stability requires that $|\lambda| \leq 1$ or, equivalently, $-1 \leq b \leq 1$.

Upon defining $\phi = \gamma \Delta t$ and $\xi = \xi_x + \xi_y$, $b$ reads

$$b = 1 - 8 \frac{(\xi_* - \xi)\,\xi}{\xi_*^2} - 2\alpha^2 \phi^2 \left[ \frac{4 \xi_x \xi_y}{\xi_*^2} + \frac{(\xi_* - 2\xi)}{\xi_*} \right] , \qquad (17)$$

where $\alpha$, $\xi_x$, $\xi_y$ and $\xi_*$ are defined in Table 2.

Putting $\phi = 0$ yields the well-known pure gravity waves problem, of which the necessary and sufficient stability condition is $\xi \le \xi_*$. When $\phi \neq 0$, for $\xi \to \xi_*/2$, one has $b = -1 - 8\,\alpha^2\phi^2\xi_x\xi_y / \xi_*^2$. It follows that numerical stability necessitates $\xi \le \xi_*/2$. Therefore, the maximum admissible time step is, at most, equal to that of pure gravity waves divided by a factor of $\sqrt{2}$. This holds true whatever the value of $\gamma$, provided $\gamma \neq 0$!

*Table 2*. Definitions of $\alpha$, $\xi_x$, $\xi_y$ and $\xi_*$ for grids A, B, C and D. One sets $(c_x, c_y) = \Delta t\,(\Delta x^{-1}, \Delta y^{-1})$. The angles $\theta_x$ and $\theta_y$ are defined to be $0 \le 2\theta_x = k_x\Delta x \le \pi$ and $0 \le 2\theta_y = k_y\Delta y \le \pi$, respectively.

| | $\alpha$ | $\xi_*$ | $\xi_x/c_x^2$ | $\xi_y/c_y^2$ |
|---|---|---|---|---|
| A grid: | 1 | 4 | $\sin^2 2\theta_x$ | $\sin^2 2\theta_y$ |
| B grid: | 1 | 1 | $\sin^2\theta_x \cos^2\theta_y$ | $\sin^2\theta_y \cos^2\theta_x$ |
| C grid: | $\lvert\cos\theta_x \cos\theta_y\rvert$ | 1 | $\sin^2\theta_x$ | $\sin^2\theta_y$ |
| D grid: | $\lvert\cos\theta_x \cos\theta_y\rvert$ | 1 | $\alpha^2 \sin^2\theta_x$ | $\alpha^2 \sin^2\theta_y$ |

*Table 3*. Necessary and sufficient von Neumann stability conditions for $\phi = 0$ (pure gravity waves) and $\phi \neq 0$ (Poincaré waves). Below, $\mu$ is such that $\sin^2\mu = c_y^2 / (c_x^2 + c_y^2)$.

| | pure gravity waves | Poincaré waves |
|---|---|---|
| A grid: | $c_x^2 + c_y^2 \le 4$ | $c_x^2 + c_y^2 \le \dfrac{2 - \phi^2 - \lvert\phi\rvert\sqrt{\phi^2 + (1-\phi^2)\sin^2 2\mu}}{1 - \phi^2 \sin^2\mu \cos^2\mu}$ |
| B grid: | $c_x^2, c_y^2 \le 1$ | $c_x^2, c_y^2 \le \dfrac{1-\phi^2}{2}$ |
| C grid: | $c_x^2 + c_y^2 \le 1$ | $\phi^2 \le 1$ and $c_x^2 + c_y^2 \le \dfrac{1}{2}$ |
| D grid: | $c_x^2, c_y^2 \le 4$ and $\dfrac{(c_x^2 + c_y^2)^3}{27\, c_x^2\, c_y^2} \le 1$ if $c_x^2 + c_y^2 \ge 6$ | unknown in general |

The stability constraints, applicable for gravity and Poincaré waves, are collected in Table 3.

As may be seen in (17), $b$ is a quadratic function of $\xi_x$ and $\xi_y$. That the stability constraint for $\phi = 0$ is different from that found for $\phi \to 0$ stems from a singular perturbation problem arising because $\phi^2$ is a multiplicative factor of $\xi_x\xi_y$, which is one of the highest degree terms of (17). An illuminating graphical interpretation thereof may be achieved.



**Graphical interpretation.** Given a fixed value of $b$ and $\alpha$, $(\xi_x, \xi_y)$ describes an elliptical path in the $(\xi_x, \xi_y)$ space. By varying $b$ one obtains concentric ellipses whose axes grow as $b$ increases. The minor axis of these ellipses lies on the symmetry axis $\xi_x = \xi_y$.

According to the stability criterion $-1 \le b \le 1$, the subspace $\xi_x, \xi_y \ge 0$ is divided into three areas, $A_-$, $A_0 = A_{0,1} \cup A_{0,2}$, and $A_+$, corresponding to $b < -1$, $-1 \le b \le 1$, and $1 < b$ (Fig. 2). The stability conditions must be such that $(\xi_x, \xi_y)$ always lies in $A_0$. Since $\xi_x$ and $\xi_y$ may vary — not necessarily independently — from 0 to their respective maxima, it is clear that $(\xi_x, \xi_y)$ cannot enter $A_{0,2}$ without crossing $A_-$. Hence, the actual stability constraint must force $(\xi_x, \xi_y)$ to remain within $A_{0,1}$. When $\phi = 0$, the $b = -1$ ellipse limiting $A_-$ transforms to a straight line so that $A_-$ vanishes: the stability area is then $A_0$, instead of $A_{0,1}$ only. This "jump" of the stability domain explains easily the fact that the stability condition changes with a discontinuity when switching from $\gamma = 0$ to $\gamma \neq 0$.

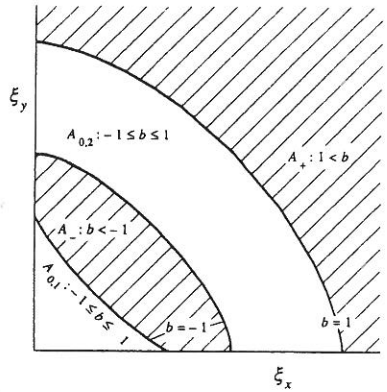


*Figure 2*. Stability and instability (hatched) regions for $0 < \phi^2 \le 1$ and $0 < \alpha$.

**Conclusion.** The example above provides a striking illustration of the fact that studying a too simple subset of equations may lead to inappropriate stability criteria. This topic has rarely been addressed, probably because of the difficulty of the relevant mathematical manipulations. Among those who have however dealt with similar problems, it is worth mentioning Cushman-Roisin (1984) or Beckers (1992).

## 4. Eddy coefficient parameterization

We now turn our attention to the problem of devising parameterizations leading to well-behaved model results. We will focus the Mellor and Yamada (1982) level 2.5 turbulence closure model.

The eddy coefficient related to a variable $a$ is given by $K_a = lqS_a$, where $l$ is the "turbulence macro-scale" and $S_a$ is a dimensionless coefficient, called a "stability function". Let the shear and the stratification be measured by the Prandtl frequency $M$ and the Brunt-Väisälä frequency

$N$, defined by $M^2 = |\partial \mathbf{u}/\partial z|^2$ and $N^2 = -\rho_0 g\, \partial\rho/\partial z$. The stability functions are functions of the dimensionless Prandtl and Brunt-Väisälä frequencies, $\tilde{M} = (lM/q)$ and $\tilde{N} = (lN/q)$. Strictly speaking, $N$ is defined for statically stable situations only, where lighter water lies on top of heavier water, so that $N^2 \geq 0$. In the present study, it is assumed that $N^2 \geq 0$ at every location and at every instant.

The eddy coefficients are thus assumed proportional to a velocity scale, $q$, and a length scale, $l$, which is that of the largest turbulent eddies, those which contain most of the turbulent kinetic energy.

The velocity and length scales obey the following evolution equations (Mellor and Yamada, 1982; Blumberg and Mellor, 1987):

$$\frac{\partial q^2}{\partial t} = 2K_u M^2 - 2K_c N^2 - \frac{2q^3}{16.6l} + \frac{\partial}{\partial z}(K_q \frac{\partial q^2}{\partial z}) + F(q^2) , \qquad (18)$$

$$\frac{\partial q^2 l}{\partial t} = 1.8lK_u M^2 - 1.8lK_c N^2 - \frac{Wq^3}{16.6} + \frac{\partial}{\partial z}(K_q \frac{\partial q^2 l}{\partial z}) + F(q^2 l) , \qquad (19)$$

I II III IV

where $K_q$ stands for the eddy viscosity relevant to the turbulence model variables. In (18)-(19), the operator $F$ accounts for the effect of advection and horizontal diffusion, if any. The wall-proximity function $W$ is a function of the turbulence macroscale as well as the distance to the sea surface and the sea bottom (*e.g.* Blumberg and Mellor, 1987). The coefficients 1.8 and 16.6 in (18)-(19) are of empirical nature, and have been determined from laboratory data. The stability functions also contain empirical coefficients and are given by

$$[S_u, S_c, S_q] = [\frac{(0.699 + 9.34\tilde{N}^2 , 0.74 + 0.902\tilde{M}^2 + 4.53\tilde{N}^2)}{1 + 5.08\tilde{M}^2 + 36.7\tilde{N}^2 + 88.8\tilde{M}^2\tilde{N}^2 + 187\tilde{N}^4} , 0.2] , \qquad (20)$$

where $S_u$, $S_c$, and $S_q$ pertain to the eddy viscosity $K_u$, the eddy diffusivity $K_c$ — generally assumed equal for all scalar variables —, and the eddy diffusivity of turbulent quantities $K_q$, respectively. The level 2.5 model should be praised for taking into account the effect on $q$ and $l$ of advection, production by shear (I), inhibition by stratification (II), viscous dissipation (III) and turbulent diffusion (IV).

In a stable environment ($N^2 \geq 0$), the vertical, turbulent flux of density generally tends to convert turbulent kinetic energy into gravitational, potential energy, thus inhibiting turbulence. By contrast, the shearing has the opposite effect: the more sheared the flow is, the more energy can be extracted from the mean flow and transformed into turbulent energy. Molecular viscosity processes, acting at scales much smaller than $l$, dissipate turbulent energy into heat.

The robustness of the level 2.5 closure — *i.e.*, its ability to produce reasonable results in a wide range of situations — has been questioned several times (Mellor and Yamada, 1982; Galperin *et al.*, 1988; Helfand and Labraga, 1988; Deleersnijder and Luyten, 1994). When $N^2$ is positive, it is believed that the stability functions, particularly $S_u$, though based on apparently sound physical basis, are mathematically ill-conditioned.

**Stability functions.** As can be seen in (20), $S_u$ and $S_c$ are decreasing function of $N^2$. Thus, if all other variables are kept fixed, any increase of $N^2$ will lead to a decrease of $K_u$ and $K_c$,



reflecting in a quite natural way the effect of stratification. On the other hand, the influence of $M^2$ on $S_u$ and $S_c$ is completely counterintuitive. Indeed, increasing $M^2$ leads to a decrease of $S_u$ and $S_c$, which may not be appropriate.

Imagine that, for some reason, $M^2$ is increasing at a given location in the domain of interest. This would lead to a decrease of $K_u$, which might allow a further increase of the shear, since the turbulent stress, $K_u \partial \mathbf{u}/\partial z$, is unlikely to exhibit wild variations. Indeed, the order of magnitude of $K_u M$ is commonly thought to be prescribed by the stress driving the turbulent boundary layer, *i.e.*, the surface wind stress or the bottom stress. Thus, a positive feedback may develop, possibly leading to a "discontinuity in the velocity" (Mellor and Yamada, 1982), which would obviously be an artefact. In other words, the velocity field may possibly present unphysical oscillations in the vertical direction.

To prevent regions of exceedingly high shear from developing, a limitation of $\tilde{M}^2$ has been considered (Mellor and Yamada, 1982), as well as a numerical filtering procedure of $\tilde{M}^2$ (Mellor, personal communication). Instead of trying to constrain, in a rather artificial way, the evolution of some variables of the turbulence model, it may seem desirable to improve the model by reappraising some of the assumptions underlying its parameterizations. This was achieved by Galperin *et al.* (1988), who devised the so-called quasi-equilibrium version of the present model. They only modified the stability functions $S_u$ and $S_c$, which are then evaluated as

$$(S_u, S_c) = (\frac{0.393 + 3.09\tilde{N}^2}{1 + 40.8\tilde{N}^2 + 212\tilde{N}^4} , \frac{0.494}{1 + 34.7\tilde{N}^2}) . \qquad (21)$$

These alternative expressions, which no longer depend on $\tilde{M}$, are referred to as "quasi-equilibrium parameterizations", for they may be obtained from the original ones by assuming — only in the stability functions — that the sources and sinks of turbulent kinetic energy balance each other. It is readily seen that, in (21), $S_u$ and $S_c$ are decreasing functions of $N^2$.

The physical basis of the modified stability functions is not better than that of the original ones. In a certain sense, it may even be deemed weaker, since more constraining assumptions are needed. Nevertheless, from a purely mathematical point of view, they are probably better conditioned.

In the quasi-equilibrium model, $q$ and $l$ are computed by means of the same evolution equations as those of the classical 2.5 model. Therefore, the main advantages of the original model are preserved, while its shortcomings are likely to be cured, as shown by the numerical experiments presented below.

**The one-dimensional model.** The well-foundedness of the parameterizations included in a model cannot be assessed by simple reasoning only. Appropriate numerical tests are obviously necessary. Accordingly, a series of numerical simulations pertaining to the surface boundary layer is carried out.

In the surface boundary layer, turbulence is partly generated by the shearing of the current, caused by the wind stress acting on the sea surface. Surface waves, when they break, also supply turbulence, a contribution which is not taken into account here. The deepening of the turbulent layer is impeded by viscous dissipation and stratification. In addition, the Coriolis force tends to limit the height of the boundary layer, even in the absence of stratification. All these phenomena are included in the model used herein.

The sea is assumed horizontally homogeneous, so that the governing equations of the problem read

$$\frac{\partial \mathbf{u}}{\partial t} + f\,\mathbf{e}_z \times \mathbf{u} = \frac{\partial}{\partial z}\left(K_u \frac{\partial \mathbf{u}}{\partial z}\right) , \tag{22}$$

$$\frac{\partial \rho}{\partial t} = \frac{\partial}{\partial z}\left(K_c \frac{\partial \rho}{\partial z}\right) . \tag{23}$$

At the initial instant, the velocity $\mathbf{u}$ is zero and the density is a linear function of $z$, $\rho(t=0,z) = (-\rho_0 N_0^2/g)z + \rho(t=0,z=0)$, where $N_0$ is the constant initial Brunt-Väisälä frequency. The fluid is set into motion by a constant stress $\tau$ applied at the sea surface: at $z = 0$, $K_u(\partial \mathbf{u}/\partial z) = \tau^s/\rho$. No mass or heat flux is imposed at the sea surface, implying that $K_c(\partial\rho/\partial z) = 0$ at $z = 0$. The surface boundary conditions for the turbulent variables are (Blumberg and Mellor, 1987) $q = 16.6^{1/3} u_*$ and $l = 0$, where $u_*$ denotes the friction velocity, defined by $u_*^2 = |\tau^s|/\rho$. We take $u_*^2 = 10^{-4}$ m$^2$ s$^{-2}$ and $N_0^2 = 10^{-4}$ s$^{-2}$.

**Discrete model.** Equations (18), (19), (22) and (23) are solved numerically by a standard finite volume technique. The only difficulty pertains to the turbulent variables: obtaining, from the numerical algorithm, negative values of $q^2$ or $q^2 l$ would be devastating. Thus, the equations of the turbulence closure model (18)-(19) must be discretized in such a way that the positivity of $q^2$ and $q^2 l$ be guaranteed.

To gain some insight into the problem of ensuring the positivity of the numerical solution of an evolution equation, let us first examine a simple model, $d\psi/dt = -D(\psi)$, where $D$, the sink term, is always positive. With an explicit time stepping, $\psi^{n+1} = \psi^n - \Delta t\, D(\psi^n)$ — where $\psi^n = \psi(n\Delta t)$, $n = 0, 1, 2...$ —, it is required that $\psi^n$ be larger than $\Delta t\, D(\psi^n)$ for $\psi^{n+1}$ to be positive. This condition may not always be verified. Patankar (1980) suggested an alternative discretization, consisting in evaluating the destruction term in a pseudo-implicit way, *viz* $D(\psi^n)\psi^{n+1}/\psi^n$. Accordingly, the modified scheme is $\psi^{n+1} = \psi^n/(1 + \Delta t D(\psi^n)/\psi^n)$, guaranteeing that $\psi^{n+1}$ is always positive — provided $\psi^n$ is positive. This scheme is simple, consistent and robust — in the sense that it is able to provide positive results, whatever the value of $\psi^n$, $D(\psi^n)$ and $\Delta t$. Consequently, Patankar (1980) pointed out, in a footnote, that "this seemingly minor topic may turn out to contain the most valuable information" in his book.

When $F$ is neglected, the equations of the closure scheme are of the form

$$\frac{\partial \psi}{\partial t} = P - D + \frac{\partial}{\partial z}\left(K_\psi \frac{\partial \psi}{\partial z}\right) , \tag{24}$$

where $\psi$ stands for $q^2$ or $q^2 l$; $P$ ($\geq 0$) and $D$($\geq 0$) denote appropriate source or sink terms.

It is desirable that the numerical scheme be able to cope with values of the dimensionless ratio $K_\psi \Delta t/\Delta z^2$ — where $\Delta z$ is the mesh size — that may be larger than 1/2. Consequently, to avoid numerical instability, an implicit discretization of the diffusion term must be implemented (*e.g.* Hirsch, 1988).

Using Patankar's (1980) trick, opting for a conservative and implicit discretization of the diffusion operator, setting $\delta^n_{k\pm1/2} = (K_\psi)^n_{k\pm1/2}\,\Delta t/\Delta z^2$, the discretized counterpart of (24) reads

$$-\delta^n_{k-1/2}\,\psi^{n+1}_{k-1} + (\delta^n_{k-1/2} + 1 + \Delta t D^n_k/\psi^n_k + \delta^n_{k+1/2})\,\psi^{n+1}_k - \delta^n_{k+1/2}\,\psi^{n+1}_{k+1}$$



$$= \psi^n_k + \Delta t P^n_k . \tag{25}$$

Therefore, the minimum value, at the new time level, of the unknown $\psi$ satisfies

$$(1 + \Delta t D^n_k/\psi^n_k)\min_k \psi^{n+1}_k = \delta^n_{k-1/2}(\psi^{n+1}_{k-1} - \min_k \psi^{n+1}_k) + \delta^n_{k+1/2}(\psi^{n+1}_{k+1} - \min_k \psi^{n+1}_k) + \psi^n_k + \Delta t P^n_k . \tag{26}$$

If the minimum value of $\psi$ is not found at a grid point adjacent to a boundary of the computational domain, then

$$\min_k \psi^{n+1}_k \geq \frac{\psi^n_k + \Delta t P^n_k}{1 + \Delta t D^n_k/\psi^n_k} \geq 0 . \tag{27}$$

The scheme may be considered positive, although there exists a slight risk that the boundary conditions be so ill-conditioned that negative values of $\psi$ may be generated. This did not occur in our simulations.

Obviously, discretizing the sink term in an explicit manner would have been less safe, especially when $\Delta t D^n_k >> \Delta t P^n_k + \psi^n_k$.

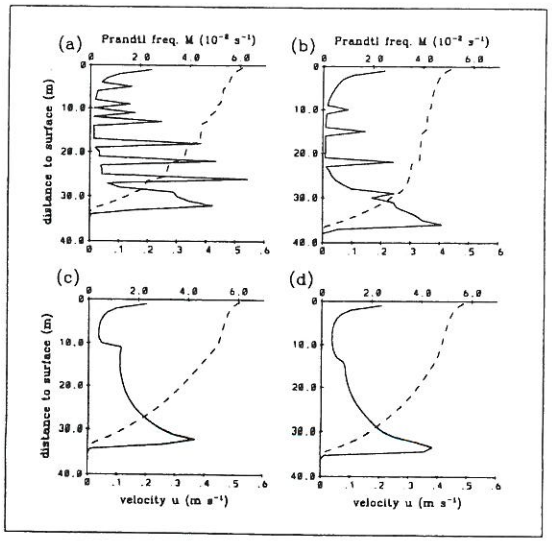


*Figure 3.* Profiles of Prandtl frequency $M$ (solid curves) and velocity (dashed curves) for $f = 0$ (no rotation) and $t = 30$ hours in the four types of numerical simulations.

**Numerical experiments.** In order to investigate the supposedly harmful influence of $M^2$ on $S_u$, four model runs are defined. The first, referred to as run (a), corresponds to the standard level 2.5 model. The experiments (b) and (c) are similar to (a), with two noticeable exceptions.

In (b), $K_u M^2 = qlS_u M^2$, appearing in the production terms of (18) and (19), is computed with the help of the quasi-equilibrium version of $S_u$. In (c), it is $K_u \partial u/\partial z = qlS_u \partial u/\partial z$ that is evaluated by resorting to the modified stability function $S_u$, as defined in (21). The quasi-equilibrium closure is used in the run (d).

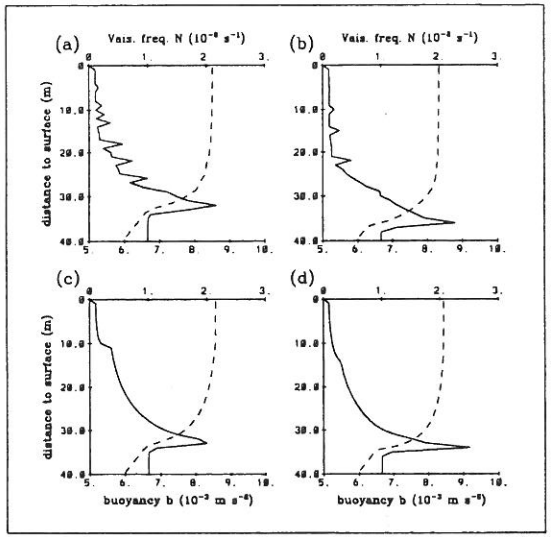


*Figure 4*. Profiles of Brunt-Väisälä frequency $N$ (solid curves) and buoyancy ($= -g(\rho - \rho_0)/\rho_0$) (dashed curves) for $f = 0$ (no rotation) and $t = 30$ hours in the four types of numerical simulations.

First, the four types of simulations are carried out with $f = 0$, a time step of $\Delta t = 120$ s, and a grid size of $\Delta z = 1$ m. When $f = 0$, laboratory data (Kato and Phillips, 1969), that may be transposed to marine scales, show that the turbulent layer depth $d_T$ may be evaluated, in a very reliable manner, as $d_T = (6/5)^{1/4} u_* N_0^{-1/2} t^{1/2}$ (Price, 1979). All simulations are limited to 30 hours, in order not to exceed the domain of validity of Price's formula (1979).

Deleersnijder and Luyten (1994) show that, in the four types of simulation, the thickness of the turbulent layer is within a few percents of Price's formula (1979). The best agreement is obtained with the quasi-equilibrium model, but this is not a decisive argument in favour of this closure scheme, for the discrepancies between the theoretical and predicted values of $d$ are rather small in all model runs.

In experiment (a), the profiles of velocity (Fig. 3a) and density (Fig. 4a) predicted by the standard model exhibit a level of noise that is certainly unphysical. The variability of $\mathbf{u}$ and $\rho$ is associated with large oscillations of the eddy viscosity and the eddy diffusivity (Fig. 5a). The results of the quasi-equilibrium closure are obviously much better, as depicted in Figs. 3d, 4d, and 5d.



The experiments (b) and (c) clearly confirm that, in accordance with the theoretical reasoning put forward above, it is solely the behaviour of the stability functions that is inadequate in the level 2.5 model. More precisely, it is $S_u$, through $K_u \partial u/\partial z$ in the momentum equation, that has the most harmful influence. Indeed, evaluating the vertical momentum flux with the quasi-equilibrium expression of $K_u$, as in experiment (c), provides much smoother results, (Figs. 3c, 4c and 5c).

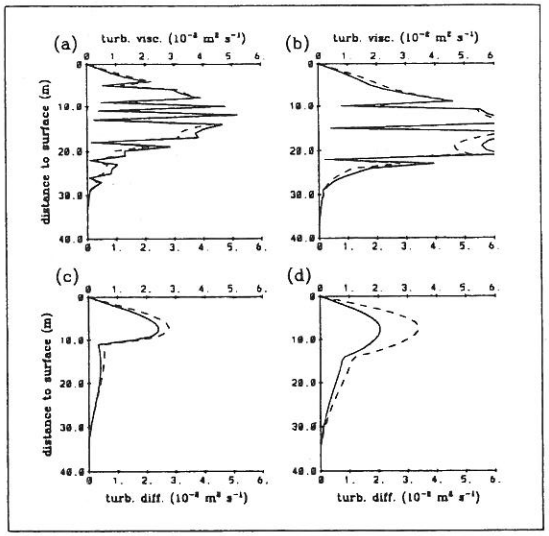


*Figure 5*. Profiles of turbulent diffusivity $K_c$ (solid curves) and turbulent viscosity $K_u$ (dashed curves) for $f = 0$ (no rotation) and $t = 30$ hours in the four types of numerical simulations.

The turbulence closure's equations (18)-(19) have source terms proportional to $K_u M^2$. In the standard level 2.5 scheme, $\partial(K_u M^2)/\partial M$ is positive. It might then be argued that any increase of the shear would lead to a growth of $ql$ that could compensate for the possible reduction of $S_u$. In the present experiments, this does not seem to occur, even when $K_u M^2$ is computed according to the quasi-equilibrium formulation of $S_u$ (Figs. 3b, 4b and 5b). In fact, in the standard model, even though $\partial(K_u M^2)/\partial M \geq 0$, $K_u M$, the norm of the turbulent stress, does not necessarily increase as $M$ increases: $\partial(K_u M)/\partial M$ is positive if $\tilde{M}^2 \leq (0.197 + 7.22\tilde{N}^2 + 36.8\tilde{N}^4)/(1 + 17.5\tilde{N}^2)$, and is negative otherwise — provided the water colum is stable ($N^2 \geq 0$). Clearly, there is the potential for any increase of $M$ to be unimpeded by the associated enhancement of the turbulent energy.

The noise present in the standard level 2.5 model is not a transient feature that would eventually disappear if one could wait for a sufficiently long time. Regions of exceedingly high shear tend to persist, despite the unsteady nature of the flow. This is illustrated in Deleersnijder and Luyten (1994).

It is worth pointing out that the pathological behaviour of the standard closure does not seem to be directly related to the mesh size. For instance, with $\Delta z = 2$ m and $\Delta z = 0.5$ m, the level 2.5 model still exhibits unacceptable oscillations, whereas the quasi-equilibrium version produces results free of unphysical noise (Deleersnijder and Luyten, 1994). With non zero Coriolis factor ($f \neq 0$), the rate of deepening of the turbulent layer is considerably slower (Mellor and Strub, 1980), but the level 2.5 model's results are still significantly less acceptable than those of the quasi-equilibrium model (Deleersnijder and Luyten, 1994).

**Conclusion.** The numerical experiments described above clearly show that ensuring the physical well-foundedness of a given parameterization is not sufficient. The stability functions tested, which seemingly are a small detail in the governing equations, may be deemed equally valid from a physical point of view, but lead to significantly different model results. One should always investigate the influence of every parameterization on the behaviour of the whole model. In general, this is not an easy task, which is no excuse for disregarding it...

## 5. Interpretation of the results of a three-dimensional marine model

In this Section, we address the problem of interpreting the large amount of information generated by a marine model. The study concentrates on the understanding of the vertical velocity field of a three-dimesional model of the region of the Berig Strait.

The Pacific and Arctic Oceans exchange mass, momentum and energy through the Bering Strait only (Fig. 6). The region of the Bering Strait exhibits some of the most intense biological productivity ever measured in the sea (Sambrotto *et al.*, 1984), with peak values that can be of the order of $10^{-2}$ kg C m$^{-2}$ day$^{-1}$. From a physical and biological point of view, this region is thus of great importance.

The monthly flow through the Bering Strait, which is of order 1 Sverdrup (= $10^6$ m$^3$ s$^{-1}$), is directed to the North, *i.e.*, from the Pacific to the Arctic. Since Coachman and Aagaard (1966), it seems clear that this northward flow is primarily induced by the water level difference between the Pacific and the Arctic. It is also believed that the variability of the flow mainly results from the wind forcing (Coachman and Aagaard, 1988). On average, two thirds of the flow pass through the Anadyr Strait.

In the domain of interest the salinity variations are predominantly horizontal, whereas the temperature contrasts are mostly observed in the vertical direction, with a marked thermocline (Coachman *et al.*, 1975). Satellite infra-red pictures show that a plume of cold water originates in the Anadyr Strait, near the Siberian coast. Although its extent depends on meso-scale phenomena, the cold water plume seems to be a permanent hydrodynamic feature (Fig. 7).

All *in situ* data analysed by Brasseur (1991) and Brasseur and Haus (1991) confirm the existence and persistence of a plume of cold water downstream of the Anadyr Strait and suggest that it is due to an intense upwelling taking place in the "Siberian half" of the Anadyr Strait. Throughout the summer period the Anadyr upwelling is likely to bring nutrients from the lower layer to the euphotic zone — where photosynthesis can take place —, continuously fuelling the primary production (Walsh *et al.*, 1989).

No device is able to directly measure vertical fluxes at reasonable cost. Moreover, indirect methods for estimating the magnitude of the vertical motions are known to be rather inaccurate.



Such considerations point to the need for a three-dimensional hydrodynamic model to compute the vertical fluxes in the domain of interest.

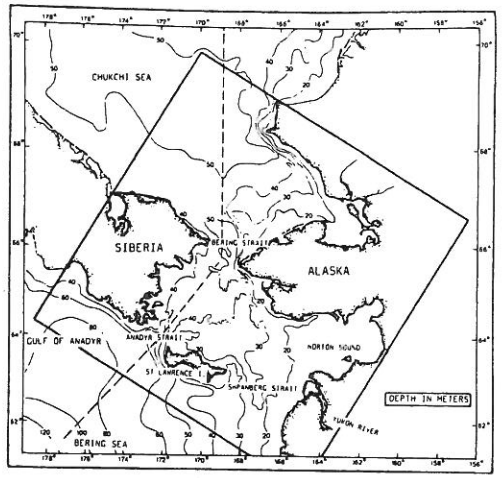


*Figure 6.* Limits of the computational domain, with bathymetry (depth in meters).

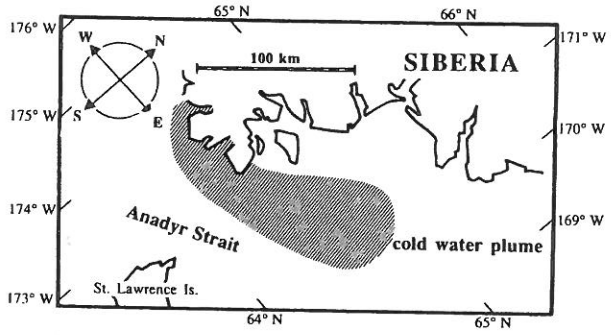


*Figure 7.* Schematic representation of the plume of cold water downstream of the Anadyr Strait.

The main objective of the hydrodynamic model study is thus the evaluation of the vertical fluxes, to test the hypothesis that it is mainly the Anadyr stream which is fuelling the huge biological production of the Bering Strait region.

**The three-dimensional model.** The hydrodynamic model study — extensively discussed in Deleersnijder (1992), Nihoul *et al.* (1993a) and Deleersnijder (1994a) — is carried out in an ecological perspective. It concentrates on the summer period, when the region of interest is virtually free of sea ice. The computational domain is a 700 km x 700 km shallow sea area, where the sea depth is $\lesssim$ 70 m (Fig. 6).

Since the ultimate aim of the study is the understanding of the biological activity, it is deemed appropriate to devote most of the attention to the general circulation, *i.e.*, the flow averaged over a sufficiently long time, say one week to one month, so that the meso-scale processes are filtered out. In the domain of interest, the general circulation is associated with much of the kinetic energy, in marked contrast to what is observed in most shelf seas.

The model set-up is described in detail in Deleersnijder (1994a). Here it is sufficient to say that the water is forced to enter the domain through the southern boundary, that steady solutions are examined, and that no wind stress is applied. Three reasons leads to neglecting the wind forcing. First, the intent is to simulate the steady state background flow, *i.e.*, the circulation free of wind-induced variability. Second, it is believed that the wind stress is not a major forcing in the domain of interest, although, over the whole Bering-Chukchi shelf, the wind stress certainly plays a major role. Third, the plume of cold water downstream of the Anadyr Strait does not seem to obey the classical wind-induced coastal upwelling scenario. Wind data indeed indicates that the wind stress is hardly ever directed so as to drive coastal upwelling (Deleersnijder, 1992). Therefore, it is found appropriate to look for an upwelling mechanism in which the wind stress has no significant role.

The equations of the model are solved numerically in the sigma-coordinate system (Phillips, 1957). Accordingly, the physical space-time coordinates are transformed to new coordinates as follows:

$$(\tilde{t}, \tilde{x}, \tilde{y}, \tilde{z} = \sigma) \;=\; (t, x, y, \frac{z + h}{\eta + h}) \;, \tag{28}$$

where $h$ and $\eta$ denote the unperturbed sea depth and the sea surface elevation, respectively. Hence, the actual height of a water column is $H = h + \eta$. In the sigma-coordinate system, the surface ($z = \eta$) and the bottom ($z = -h$) of the sea are coordinate surfaces. The latter is defined as $\sigma = 0$, while the former corresponds to $\sigma = 1$.

Along with the transformed vertical coordinate $\sigma$, it is customary to use a new vertical velocity, defined as $\tilde{w} = D_t\,\sigma$, where $D_t$ represents the material derivative operator, *i.e.*, $D_t = \partial/\partial t + \mathbf{u}\bullet\nabla + w\,\partial/\partial z$. With the transformed vertical velocity, the impermeability of the surface and the bottom is easily taken into account by prescribing $\tilde{w} = 0$ at $\sigma = 1, 0$.

In the sigma-space, the generic equation (7) is transformed to

$$H^{-1}\left[\frac{\partial(H\psi)}{\partial\tilde{t}} + \tilde{\nabla}\bullet(H\,\mathbf{u}\,\psi) + \frac{\partial(H\tilde{w}\,\psi)}{\partial\sigma}\right] = Q^{\psi} + H^{-1}\,\tilde{\nabla}\bullet(H\,A_{\psi}\,\tilde{\nabla}\psi) + H^{-2}\,\frac{\partial}{\partial\sigma}(K_{\psi}\,\frac{\partial\psi}{\partial\sigma}) \;, \tag{29}$$



with $\tilde{\nabla} = \mathbf{e}_x\partial/\partial\tilde{x} + \mathbf{e}_y\partial/\partial\tilde{y}$. The generic equation (29) is not more complicated than (7). Following Mellor and Blumberg (1985), the horizontal diffusion term has not been transformed to its exact sigma-coordinate counterpart. In fact, a much simpler expression is chosen (Deleersnijder and Wolanski, 1990; Deleersnijder, 1992).

The equations are discretized, in the sigma space, according to the finite volume technique (Peyret and Taylor, 1983). The grid size is 10 km in both horizontal directions, and each water column is divided into 10 sigma-levels. The vertical eddy diffusivities are computed from a turbulence closure which is similar to that described in Section 4, except that the turbulence macro-scale is obtained from an algebraic, empirical formula, and that the stability functions are those of Nihoul and Djenidi (1987) (see also Deleersnijder, 1992). According to an appropriate model calibration procedure, the horizontal viscosity $A_u$ is taken to be 500 $m^2\,s^{-1}$, while the horizontal diffusivity is $A_c = 75\ m^2\,s^{-1}$.

**Upsloping and upwelling.** In the sigma coordinate, the equations of the model do not explicitly involve the "physical" vertical velocity $w$. Computing the latter is then part of the postprocessing of the model results.

As suggested by Waleffe (1985) and Deleersnjder (1989), it is useful to split $w$ into two contributions, $w = w_{US} + w_{UW}$.

The upsloping velocity, $w_{US}$, reads

$$w_{US} \;=\; \sigma\,\frac{\partial\eta}{\partial t} - \mathbf{u}\bullet[\,(1-\sigma)\nabla h - \sigma\nabla\eta\,] \;. \tag{30}$$

It may be seen that a particle moving with a velocity equal to $\mathbf{u} + w_{US}\mathbf{e}_z$ does not cross any iso-$\sigma$ surface, implying that this particle remains at the same relative height in the water column. Since the bottom and the surface are iso-$\sigma$ surfaces, $w_{US}$ may be regarded as the vertical velocity adapted to the slope of the surface and the bottom. Since the present analysis pertains to steady state model results, the first term in the right-hand member of (30) is zero.

The upwelling velocity,

$$w_{UW} \;=\; H\tilde{w} \;, \tag{31}$$

is the velocity with which the water crosses the iso-$\sigma$ surfaces. Therefore, $w_{UW}$ may be interpreted as the vertical velocity associated with proper up- or down-welling motions.

This decompositon of the vertical velocity provides an interesting analysis tool, for it renders it possible to distinguish between the part of the vertical velocity that is necessary for the flow to accommodate to the geometry of the basin and the extra vertical velocity related to actual up- or down-wellings.A significant drawback must nevertheless be highlighted. Definitions (30) and (31) are purely arbitrary: it is indeed possible to put forward several alternative expressions of $w_{US}$ and $w_{UW}$ that could be equally valid as regards the distinction between the vertical motions that are associated with the geometry of the basin and those that are not. What justifies (30) and (31) is only that they take advantage in a very natural way of the use of the sigma-coordinate system. In a certain sense, (30) and (31) are inherent in the sigma-transformation.

In accordance with the present reasoning, we will examine separately the upsloping and upwelling velocities.

To understand the space distribution of the upsloping velocity, it is desirable to identify the dominant terms of definition (30). The sea surface elevation does not exceed $\pm$ 0.4 m

(Deleersnijder, 1992). Hence, in (30), $\sigma\nabla\eta$ may be neglected compared with $(1-\sigma)\nabla h$. Let $\hat{\mathbf{u}} = \mathbf{u} - \bar{\mathbf{u}}$ denote the deviation of the horizontal velocity relative to its depth-average $\bar{\mathbf{u}}$ (Fig 8). Model results indicate that, roughly speaking, $|\hat{\mathbf{u}}| \approx 0.1\ |\bar{\mathbf{u}}|$ (Fig. 9) (Deleersnijder, 1992). It is thus suggested that $w_{US}$ be approximated by a "simplified upsloping velocity" defined as $w_{US,S} = -(1-\sigma)\,\bar{\mathbf{u}}\bullet\nabla H$, which may be transformed to an expression better suited to numerical calculations, *viz* $w_{US,S} = (1-\sigma)\,H\,\nabla\bullet\bar{\mathbf{u}}$, by using the — steady state — depth-integral of the continuity equation $\nabla\bullet(H\bar{\mathbf{u}}) = 0$.

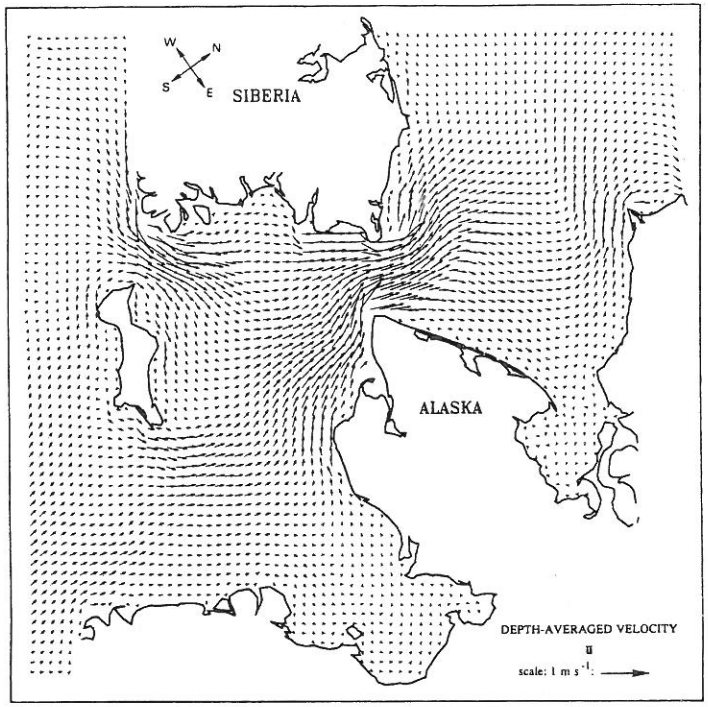


*Figure 8.* Depth-averaged horizontal velocity field computed by the model.

The modelled horizontal velocity field was shown to be in good agreement with the available measurements (Deleersnijder, 1992; Nihoul *et al.*, 1993a). The latter do not however permit the evaluation of the vertical shear in a reliable way, because there were hardly ever several currentmeters on the same vertical. Nevertheless, the available dataset loosely suggests that $\hat{\mathbf{u}}$ is much smaller than $\bar{\mathbf{u}}$.



The simplified upsloping velocity turns out to be reasonably close to $w_{US}$. Indeed, upon denoting $|r|_{rms}$ the root mean square taken over the whole computational domain of a variable $r$, one has $|w_{US,S} - w_{US}|_{rms} / |w_{US}|_{rms} = 0.24$, which means that $w_{US,S}$, roughly speaking, accounts for 76% of $w_{US}$.

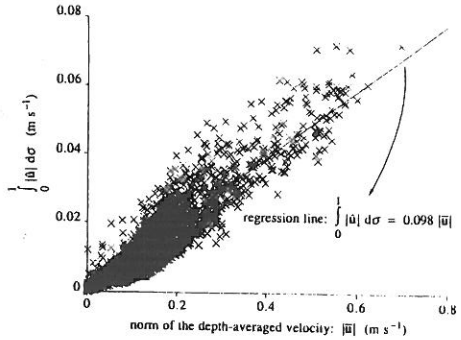


*Figure 9.* Scatterplot displaying, for each wet vertical, the depth-average of $|\hat{\mathbf{u}}|$ as a function of $|\bar{\mathbf{u}}|$.

The most advantageous feature of the simplified upsloping velocity is that, over each water column, the values of $w_{US,S}$ are self-similar: $|w_{US,S} / (H\nabla\bullet\bar{\mathbf{u}})|$ is a linear function of $\sigma$ only, which is zero at the surface and maximum at the bottom.

Since $w_{US}$ is close to $w_{US,S}$, the vertical profiles of the upsloping velocity are nearly self-similar. As a result, to interpret the three-dimensional field of upsloping velocity, it is sufficient to display a depth-independent quantity such as, for instance, the depth-mean upsloping velocity $\bar{w}_{US}$ (Fig. 10). It would be less appropriate to simply display the upsloping velocity in a series of horizontal planes of section located at various depths below the surface. Doing that would result in confusing pictures in which it would be difficult to distinguish between the horizontal variablity of $w_{US}$ that is intrinsic to the flow and that associated with the plane of section being, from one location to another, relatively closer or more distant to the sea surface or bottom.

Looking simultaneously at Figs. 6, 8 and 10, one immediately sees that, as expected, the upsloping velocity is positive where the flow is directed towards shallower regions and is negative otherwise. Furthermore, $|\bar{w}_{US}|$ is maximum in the vicinity of Anadyr and Bering Straits, *i.e.*, in the regions where the horizontal current most clearly crosses the isobaths while having a large speed. In particular, the upsloping velocity is high in the Anadyr Strait, indicating significant upwards water fluxes.

It must be pointed out that the upsloping velocity cannot bring a water parcel up to the surface. However, when the upsloping velocity is positive, every water parcel comes closer to the surface, while remaining at the same relative height in the water column. This may render it more likely for the turbulent diffusion to mix some of the water column, or even the whole

water column, since the height of fluid to be mixed decreases. Whether or not this hypothesis is correct is difficult to verify, because this mechanism involves two processes interacting non-linearly. Anyway, this process, if it actually exists, could be responsible for part of the cold water plume developing downstream of the Anadyr Strait.

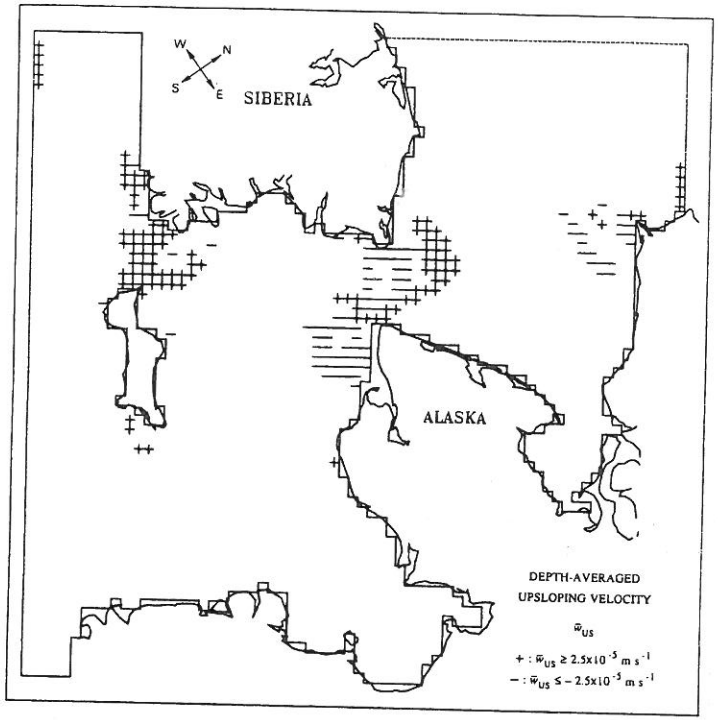


*Figure 10.* Depth-averaged upsloping velocity field. The verticals where $\bar{w}_{US} \geq 2.5\text{x}10^{-5}$ m s$^{-1}$ ($\bar{w}_{US} \leq 2.5\text{x}10^{-5}$ m s$^{-1}$) are identified by "+" ("–").

According to the model results (Deleersnijder, 1992), most vertical profiles of $w_{UW}$ are of the same type: as $\sigma$ increases from 0 to 1, $|w_{UW}|$ grows from zero at the bottom, reaches a maximum and finally decreases to zero at the surface. However, the location of the maximum of $|w_{UW}|$ may vary very widely from one vertical to another. Although the vertical profiles of $w_{UW}$ may not be regarded as approximately self-similar, they exhibit enough common features for a method resembling that used to display $w_{US}$ to be feasible for the graphical representation of the field of upwelling velocity (Fig. 11).

Significant up- and down-wellings are found in small areas. Upwelling phenomena taking place in the one-grid-box-wide strip along the southern open boundary clearly correspond to an



artefact due to improper boundary conditions imposed on the horizontal velocity (Deleersnijder, 1992). In the region of the Anadyr Strait, close to the Siberian coast, the upwelling velocity is directed upwards and can be as high as 10 m day$^{-1}$. Thus, the upwelling velocity is large enough to bring the thermocline, initially located at $z = -15$ m, up to the surface.

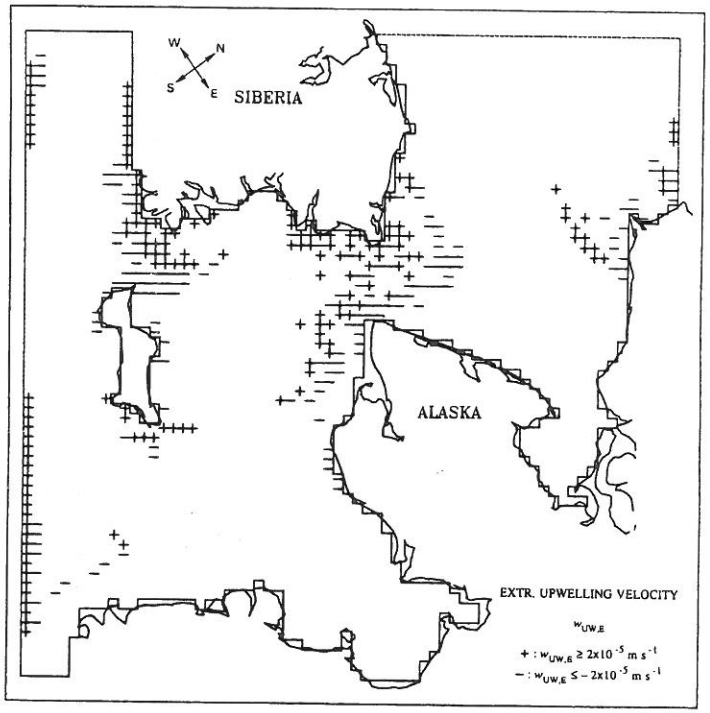


*Figure 11.* Representation of the upwelling velocity. For each water column, one takes into account the extremum of the upwelling velocity, $w_{UW,E}$, *i.e.*, the value of $w_{UW}$ that has the maximum absolute value. The verticals where $w_{UW,E} \geq 2\text{x}10^{-5}$ m s$^{-1}$ ($w_{UW,E} \leq 2\text{x}10^{-5}$ m s$^{-1}$) are identified by "+" ("–").

As previously stated, the wind forcing is not the main cause of the vertical motions. It follows that one has to look for another upwelling mechanism. Inspiration can be found in the Ekman pumping theory set out in classical treatises of geophysical fluid mechanics (*e.g.*, Cushman-Roisin, 1994).

It may be seen that

$$w_{UW} = -\int_0^\sigma \tilde{\nabla}\bullet(H\,\hat{\mathbf{u}})\;d\sigma\;. \qquad (32)$$

Consequently one has to analyse the behaviour of $H\hat{\mathbf{u}}$ in order to understand the distribution of $w_{UW}$.

The direction of $\mathbf{u}$ with respect to $\bar{\mathbf{u}}$ is measured by the angle $\beta$, which may be calculated from $\sin\beta = \mathbf{e}_z\bullet(\bar{\mathbf{u}}\times\mathbf{u}) / (|\bar{\mathbf{u}}|\,|\mathbf{u}|)$. Angle $\beta$ is positive if $\mathbf{u}$ is "on the left of $\bar{\mathbf{u}}$", and is negative otherwise. For each water column, the veering $\Xi$ is defined as $\Xi = \beta_{max} - \beta_{min}$, if the point where $\beta = \beta_{max}$ is closer to the bottom than that where $\beta = \beta_{min}$. Otherwise, $\Xi = \beta_{min} - \beta_{max}$. The mean veering is about 12°. The veering is positive in 2556 verticals out of a total of 2690. In 95% of the verticals of the computational domain, the direction of $\mathbf{u}$ is qualitatively in agreement with that of the bottom Ekman spiral, *i.e.*, $\mathbf{u}$ is on the left of $\bar{\mathbf{u}}$ near the bottom and on the right near the surface.

The qualitative properties of $H\hat{\mathbf{u}}$ are accounted for in the following Taylor expansion of $H\hat{\mathbf{u}}$ truncated at two terms:

$$H\,\hat{\mathbf{u}} = (H\,\hat{\mathbf{u}})_{//} + (H\,\hat{\mathbf{u}})_{\perp}\;, \qquad (33)$$

with

$$[(H\,\hat{\mathbf{u}})_{//}, (H\,\hat{\mathbf{u}})_{\perp}] = (1-2\sigma)\,[-a_{//}, a_{\perp}\,\mathbf{e}_z\times]\,H\bar{\mathbf{u}}\;, \qquad (34)$$

where $a_{//}$ and $a_{\perp}$ are positive constants. Relations (33) and (34) are by no means intended to provide a reliable approximation to the vertical profiles of $H\hat{\mathbf{u}}$. Instead, (33)-(34) are simply intuitively appealing formulae having some of the modelled properties of $H\hat{\mathbf{u}}$: in (33)-(34), the depth average of $|\hat{\mathbf{u}}|$ is a linearly increasing function of $|\bar{\mathbf{u}}|$ (Fig. 9), and the veering is always positive.

Let $w_{UW,//}$ and $w_{UW,\perp}$ denote the upwelling velocity related, through (32), to $(H\,\hat{\mathbf{u}})_{//}$ and $(H\,\hat{\mathbf{u}})_{\perp}$, respectively. Accordingly, $w_{UW} = w_{UW,//} + w_{UW,\perp}$.

Introducing the two contributions to the transport $H\hat{\mathbf{u}}$ defined in (34), taking the depth-integrated continuity equation, $\nabla\bullet(H\bar{\mathbf{u}}) = 0$, into account, it is readily seen that $w_{UW} = w_{UW,\perp}$ and $w_{UW,//} = 0$. The same calculations may be carried out with the modelled field of $H\hat{\mathbf{u}}$. To do so, the following definitions are introduced

$$[(H\,\hat{\mathbf{u}})_{//}, (H\,\hat{\mathbf{u}})_{\perp}] = |\bar{\mathbf{u}}|^{-2}\;[\,\hat{\mathbf{u}}\bullet\bar{\mathbf{u}}\;,\;(\hat{\mathbf{u}}\bullet(\mathbf{e}_z\times\bar{\mathbf{u}}))\,\mathbf{e}_z\times\,]\;H\bar{\mathbf{u}}\;. \qquad (35)$$

The corresponding upwelling velocities may then be evaluated. According to the model results, the latter obey

$$[\,|w_{UW,//} - w_{UW}|_{ms}\,,\,|w_{UW,\perp} - w_{UW}|_{ms}\,] = [0.72,\;0.28]\;(\,|w_{UW,//}|_{ms} + |w_{UW,\perp}|_{ms}\,)\;, \qquad (36)$$

where, for a given variable $s$, $|s|_{ms}$ represents $(|s|_{rms})^2$. This clearly supports the well-foundedness of the splitting (34), for the modelled upwelling velocity is mostly associated with the variations of $(H\,\hat{\mathbf{u}})_{\perp}$, while the role of $(H\,\hat{\mathbf{u}})_{//}$ is less important in this respect.



Another type of analysis is suggested by the idealized form (34). Combining (32)-(34) yields $w_{UW} = a_{\perp}\,\mathbf{e}_z\bullet(\nabla\times H\bar{\mathbf{u}})\;\sigma(1-\sigma)$, implying

$$\mathrm{sign}(\bar{w}_{UW}) = \mathrm{sign}[\mathbf{e}_z\bullet(\nabla\times H\bar{\mathbf{u}})]\;, \qquad (37)$$

where $\bar{w}_{UW}$ represents the depth-average of the upwelling velocity.

Whether or not the sign of the upwelling velocity is actually given by the sign of the curl of the transport $H\bar{\mathbf{u}}$ is easily checked. It turns out that (37) provides an excellent account of the model results (Table 4).

*Table 4.* Assessment of (37): $n_+$ denotes the number of water columns where the sign of the depth-averaged upwelling velocity is equal to that of $\mathbf{e}_z\bullet(\nabla\times H\bar{\mathbf{u}})$, while $n_-$ is the number of verticals where (37) does not apply; $\bar{w}_{UW}$ is expressed in $10^{-5}$ m s$^{-1}$.

| | $n_+$ | $n_-$ | $\frac{n_+}{n_+ + n_-}$ |
|---|---|---|---|
| $\lvert\bar{w}_{UW}\rvert \geq 0.1$ | 1547 | 315 | 0.83 |
| $\lvert\bar{w}_{UW}\rvert \geq 1$ | 240 | 69 | 0.78 |
| $\lvert\bar{w}_{UW}\rvert \geq 3$ | 30 | 3 | 0.91 |
| $\lvert\bar{w}_{UW}\rvert \geq 5$ | 10 | 1 | 0.91 |
| $\lvert\bar{w}_{UW}\rvert \geq 7$ | 1 | 0 | 1.00 |
| $\lvert\bar{w}_{UW}\rvert \geq 9$ | 0 | 0 | |

The mechanism of the up- and down-wellings illustrated here is probably the following. The main driving force of the horizontal velocity is the part of the pressure force that is associated with the gradient of the sea surface elevation. Due to frictional forces associated with the bottom stress, the horizontal velocity is not identically equal to its depth-average. Moreover, the Coriolis force induces a positive veering of the velocity. The resulting space variations of $(H\hat{\mathbf{u}})_{\perp}$, correlated with those of $H\bar{\mathbf{u}}$, lead to local divergence or convergence of $H\hat{\mathbf{u}}$, implying vertical motion in the sigma-space. The variations of $(H\hat{\mathbf{u}})_{//}$ have less impact on the upwelling velocity.

What has been done above simply amounts to adapting the Ekman pumping theory to our results, where the bottom stress turns out to be the ultimate cause of the vertical motions.

**Flow dynamics.** The above analysis of the velocity field has mostly been "kinematic". It is appropriate to address some dynamical aspects. In particular, it is crucial to understand why the veering is overwhelmingly positive.

By virtue of the hydrostatic equilibrium, the horizontal pressure gradient force reads

$$-\rho_0^{-1}\nabla p = -g\,\nabla\eta - \rho_0^{-1}\nabla\int_z^\eta \rho\,g\;dz\;. \qquad (38)$$

Owing to the relative smallness of the sea depth and the horizontal density gradients, the last term of (38) is negligible compared with $-g\,\nabla\eta$, the pressure force due to the slope of the sea surface (Deleersnijder, 1992).

On the other hand, the acceleration term $\nabla\bullet(\mathbf{uu})$ is generally much smaller than the Coriolis term. This may be verified by evaluating the Rossby number,

$$Ro = \frac{U}{fL} \approx \frac{|\nabla\bullet(\mathbf{uu})|}{|f\,\mathbf{e}_z \times \mathbf{u}|} , \tag{39}$$

where $U$ and $L$ denote the horizontal velocity and length scales, respectively. In view of the domain (Fig. 6), one takes $L \approx 30$ km. It seems quite natural to prescribe $V \approx |\mathbf{u}|_{rms} \approx 0.2$ m s$^{-1}$. Bearing in mind that $f \approx 10^{-4}$ s$^{-1}$, one has $Ro \approx 0.07$.

The magnitude of the horizontal diffusion term relative to the Coriolis force is measured by the horizontal Ekman number,

$$Ek = \frac{A_u}{fL^2} \approx \frac{|\nabla\bullet(A_u\,\nabla\mathbf{u})|}{|f\,\mathbf{e}_z \times \mathbf{u}|} . \tag{40}$$

It is readily seen that $Ek \approx 0.006$, implying that, for the basin-scale motions, the horizontal diffusion of momentum is negligible. However, the two-grid interval noise, the length scale of which is $L \approx \Delta x/\pi \approx 3$ km, is significantly affected by the horizontal diffusion operator. At this scale, one indeed has $Ek \approx 0.5$. As a consequence, the horizontal diffusion efficiently smoothes the small-scale computational noise, while leaving relatively unaffected the meaningful scales of motions.

This order of magnitude analysis implies that the dominant part of the horizontal momentum equation is

$$-f\,\mathbf{e}_z \times \mathbf{u} - g\,\nabla\eta + \frac{\partial}{\partial z}\left(K_u \frac{\partial \mathbf{u}}{\partial z}\right) \approx 0 , \tag{41}$$

as verified in Deleersnijder (1992). The latter equation is often called "Ekman equation".

All closed form solutions to (41), obtained in idealized cases — generally with $K_u$ = const. —, exhibit a positive veering in the Northern Hemisphere, where $f > 0$ (*e.g.* Cushman-Roisin, 1994). This turns out to be reassuring as to the well-foundedness of the analysis carried out in this lecture. It is however desirable that the positivity of the veering be understood by means of a more general rationale.

Let $\tau = \rho_0 A_V^u \partial\mathbf{u}/\partial z$ denote the stress due to the turbulent, vertical flux of horizontal momentum. Bearing in mind that no wind stress is applied at the sea surface, *i.e.*, $\tau(\sigma=1) = 0$, the depth-average of (41) reads

$$-f\,\mathbf{e}_z \times \bar{\mathbf{u}} - g\,\nabla\eta - (\rho_0 H)^{-1}\,\tau^b \approx 0 , \tag{42}$$

where $\tau^b = \tau(\sigma=1)$ is the turbulent stress exerted by the fluid on the sea bottom. Substracting (42) from (41) yields

$$-f\,\mathbf{e}_z \times \hat{\mathbf{u}} + (\rho_0 H)^{-1}\left(\frac{\partial \tau}{\partial \sigma} + \tau^b\right) \approx 0 . \tag{43}$$



Near the sea bed, there is a thin boundary layer in which the velocity goes to zero — as the bottom is approached — according to a logarithmic profile (*e.g.* Wimbush and Munk, 1971). This boundary layer is not resolved by the numerical model, so that the modelled horizontal velocity is not prescribed to be zero at the sea bed. Rather, a slip boundary condition is resorted to, whereby the bottom stress is evaluated as $\tau^b = \rho_0 C_D |\mathbf{u}(d)|\,\mathbf{u}(d)$, where $C_D$ and $d$ represent an appropriate drag coefficient ($C_D \approx 0.002$) and the distance to the bottom of the first grid point where $\mathbf{u}$ is computed, respectively. Since $|\hat{\mathbf{u}}| << |\bar{\mathbf{u}}|$, it is clear that $\tau^b$ is approximately equal to $\rho_0 C_D |\bar{\mathbf{u}}|\,\bar{\mathbf{u}}$. Upon defining $\mathbf{e}$ as the unit vector parallel to $\bar{\mathbf{u}}$, *i.e.*, $\mathbf{e} = \bar{\mathbf{u}}/|\bar{\mathbf{u}}|$, it is very likely that

$$\tau^b \bullet \mathbf{e} > 0 . \tag{44}$$

Let $(\hat{u}_\perp, \tau_{//}, \tau^b_{//}) = \mathbf{e}\bullet(-\mathbf{e}_z \times \hat{\mathbf{u}}, \tau, \tau^b)$. The dot product of $\mathbf{e}$ and equation (43) leads to

$$f\,\hat{u}_\perp + (\rho_0 H)^{-1}\left(\frac{\partial \tau_{//}}{\partial \sigma} + \tau^b_{//}\right) \approx 0 . \tag{45}$$

The stress component $\tau_{//}$ decreases from $\tau^b_{//}$ at the bottom to zero at the sea surface. It is convenient to assume that the decay of $\tau_{//}$ is monotonic, requiring that $\partial\tau_{//}/\partial\sigma \le 0$. If, for example, $\tau_{//}$ decreases linearly as the surface is approached, *i.e.*, $\tau_{//} = (1-\sigma)\,\tau^b_{//}$, then $\hat{u}_\perp = 0$. But, the latter hypothesis is not likely to be valid. In the idealized closed-form solutions, the stress generally obeys an exponential law. In the flow under study, the stress is nearly zero at the pycnocline, for the stratification prevents large turbulent fluxes. Since the pycnocline is generally located well below the sea surface, $\tau_{//}$ must decrease faster than a linear function of $\sigma$.

In the light of the arguments put forward above, it is conceivable that

$$\frac{\partial \tau_{//}}{\partial \sigma} + \tau^b_{//} < 0 , \quad \text{near the bottom,} \tag{46a}$$

$$\frac{\partial \tau_{//}}{\partial \sigma} + \tau^b_{//} > 0 , \quad \text{near the surface.} \tag{46b}$$

As a result,

$$\hat{u}_\perp > 0 , \quad \text{near the bottom,} \tag{47a}$$

$$\hat{u}_\perp < 0 , \quad \text{near the bottom.} \tag{47b}$$

The latter inequalities are in agrement with the fact that $\hat{u}_\perp$, having zero depth-mean, must exhibit at least one zero on every water column. Furthermore, (47a) and (47b) strongly suggest that a positive veering prevails, which must indeed be the case when $\hat{u}_\perp$ only has one zero.

Equations (41) and (42) do not clearly support the hypothesis that $|\hat{\mathbf{u}}|$ should scale as $|\bar{\mathbf{u}}|$. In fact, various scaling arguments may be equally relevant, leading to linear or quadratic laws (Deleersnijder, 1992). Moreover, it is not clear at all that $\hat{\mathbf{u}}_{//}$ and $\hat{\mathbf{u}}_\perp$ should scale in a similar way. Finally, $H$ should play some role in this order of magnitude analysis. Therefore, it may be concluded that the dynamics of the flow agrees with $|\hat{\mathbf{u}}|$ being an increasing function of $|\bar{\mathbf{u}}|$, but assuming a linear law, independent of the depth, is certainly an over-simplification, which has however proved very fruitful in the preceding section.

Overall, the kinematic arguments resorted to for gaining insight into the upwelling mechanism are seemingly in accordance with the momentum budget, although there remain some minor discrepancies.

**Conclusion.** The interpretation methods used above have been able to reduce, by hefty dose of physical intuition, three-dimensional results to two-dimensional plots, "rms" figures or simple, short, analytic formulae, such as (37). Synthetic information has thus been obtained from the 26,900 grid nodes where the flow field variables are discretized.

The analysis technique of the vertical velocity, based on the distinction between upsloping and upwelling velocity fields, has been shown to work rather well for two main reasons. First, upsloping and upwelling are very different processes. Second, the typical profiles of the corresponding vertical velocities are completely dissimilar.

The vertical velocity field produced by the model in the vicinity of the Anadyr Strait is qualitatively in agreement with the observations. According to the results of the model, the Anadyr Strait plume of cold water is caused by an upwelling process, possibly combined with upsloping and turbulent diffusion. The upwelling mechanism identified in the simulated currents closely resembles the classical Ekman pumping process, which is a concept generally applied to the surface or bottom boundary layers in deep seas. It is proposed that the notion of shallow-sea Ekman pumping be introduced, as a process concerning the whole water column.

The velocity field discussed above has been used as an input to an ecological model, confirming the crucial role of the Anadyr Strait upwelling in fuelling the primary production (Adam, 1990; Nihoul *et al.*, 1993b).

## 6. Some results of a World Ocean model

Another problem of interest is that of predicting the evolution of the Earth's climate under natural and anthropogenic forcings.

Mankind is currently conducting an "experiment" with the global climate. Each year, billions of tons of carbon dioxide, an acknowledged greenhouse gas, are released into the atmosphere, primarily as a result of the combustion of fossil fuels, *i.e.*, coal, oil or gas. Other greenhouse gases, namely methane, nitrous oxide and chlorofluorocarbons, are also being released. Large amounts of these gases remain in the atmosphere, so that the atmospheric concentration in greenhouse gases is increasing, which will significantly alter the Earth's climate. In a few decades, the global temperature may increase to a level unprecedented in the recorded history of mankind (Houghton *et al.*, 1990; Houghton *et al.*, 1992). It is believed that all human activities will be affected, directly or indirectly, by any warming of the atmosphere — even of a few degrees — and any associated modification of the rainfall.

Mathematical models are the only tools that can take up the challenge of predicting future climates.

The Earth's climate system consists of the atmosphere, the hydrosphere, the cryosphere, the surface lithosphere and the biosphere. These components have quite different physical characteristics and time scales, and are linked to each other and to conditions external to the system by a variety of physical processes. Ideally, climate models should treat all these components in an interactive way, which is virtually impossible today, since the power of the available computers is not sufficient.



Predicting, with an acceptable degree of realism, the evolution of climate on time scales of a few decades can be achieved with a model incorporating only representations of the atmosphere, ocean and sea-ice sub-systems. At Louvain-la-Neuve, we are developing such a model of the climate system, and some results of the oceanic component will be presented below.

**The model.** As pointed out by Niiler (1992), "the principal role of the oceans in maintaining the present climate system of the Earth is the creation of large reservoirs of heat in tropical latitudes and the transport of this thermal energy to the polar latitudes". Throughout the year, the World Ocean transports about $10^{15}$ W — in thermal energy — from the low latitudes toward the poles (*e.g.* Hastenrath, 1982), which is somewhat smaller than the meridional atmospheric heat transport. Thus, by removing heat from the tropics and carrying it toward the poles, the World Ocean significantly reduces the equator-poles contrasts. In addition, because of their large heat capacity, the upper layers exhibit a large thermal inertia, moderating the amplitude of the surface temperature seasonal cycle (*e.g.* Monin, 1975). Finally, the World Ocean may act as a sink of carbon dioxide (*e.g.* Sarmiento, 1992).

The Louvain-la-Neuve Ocean General Circulation Model (OGCM) is rather similar to the most classical OGCMs (*e.g.* Bryan, 1969). It is based on the usual set of assumptions, *i.e*, the hydrostatic equilibrium and the Boussinesq approximation. The prognostic variables are the sea surface elevation, the three components of the velocity, the potential temperature and the salinity. The turbulence closure is achieved according to the simple formulae of Pacanowski and Philander (1981). The space discretization uses the finite volume technique on an Arakawa B-grid. The time stepping is of Euler-forward type, with a split-explicit mode splitting to circumvent the severe numerical stability constraints associated with the propagation of external inertia-gravity waves (Gadd, 1978; Killworth *et al.*, 1991; Deleersnijder and Campin, 1995).

More details about our OGCM may be found in Deleersnijder and Campin (1993, 1995) and in the Appendix. Hereafter, the curvilinear coordinate system underlying the horizontal discretization is discussed.

**Horizontal curvilinear coordinate system.** In most OGCMs, the numerical grid is based on the standard spherical coordinate system, which has singularities at both the North Pole and the South Pole. As those singularities are approached, the latitudinal grid size tends to zero, which may lead to numerical instabilities. Since the South Pole is located sufficiently far away from the nearest oceanic region, the reduction of the latitudinal grid size has no harmful effect. Thus, it is only in the Arctic Ocean that the grid or the numerical method has to be adapted to circumvent this numerical instability problem.

Several methods to deal with the singularities of the spherical coordinates have been examined (*e.g.* Williamson, 1979). Fourier-filtering along the longitudinal direction is used in many OGCMs, in spite of the potential problems that may arise because not all the grid points along a latitudinal circle are active.

Some years ago, the LODYC (Laboratoire d'Océanographie Dynamique et de Climatologie, Paris) model has been adapted to an orthogonal curvilinear grid obtained by shifting the northern singularity into a land region, located in the neighbourhood of the North Pole (Marti *et al.*, 1990; Marti *et al.*, 1992)

Another modification of the standard spherical coordinate system has been suggested (Deleersnijder *et al.*, 1993; Eby and Holloway, 1994; Coward *et al.*, 1995), consisting in

combining two spherical sub-grids in such a way that their singularities are not close to their own wet grid points. The first sub-grid, $G$, covering the Southern Hemisphere, the Indian Ocean, and the Pacific Ocean up to the Bering Strait, is based on geographical spherical coordinates. The second sub-grid, $G'$, is associated with spherical coordinates having their poles on the Equator. This second grid encompasses the Northern Hemisphere part of the Atlantic together with the Arctic Ocean. The two sub-grids are connected to each other in the equatorial Atlantic. With this technique, there is thus no singular point, neither in $G$, nor in $G'$ (Fig. 12).

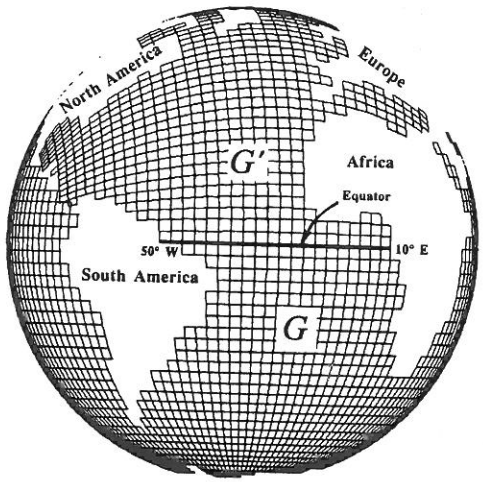


*Figure 12.* Illustration of the two-grid system, with the connection line in the equatorial Atlantic (courtesy Jacques Haus).

Instead of solving the equations of the model separately on the two sub-grids — with appropriate matching of the fluxes across the connection line —, we consider the two spherical coordinate systems as a single, orthogonal, curvilinear coordinate system. This way, the computational domain does not have to be viewed as a set of two sub-domains. On the other hand, however, the governing equations must be written — and solved — in a curvilinear coordinate system, which is slightly more complicated.

The North Pole of $G'$ is located on the geographical equator at longitude $\theta \approx 70°$, *i.e.*, in the Indian Ocean (Deleersnijder *et al.*, 1993). Let $a$, $\lambda$ and $\phi$ denote the Earth's radius, the geographical longitude and latitude, respectively. If $\lambda'$ and $\phi'$ represent the longitude and latitude in the spherical coordinate system on which $G'$ is based, it may be shown that (Deleersnijder *et al.*, 1993)



$$(\lambda - \theta, \phi) = [\, -\mathrm{atan}(\sin\lambda' \cot\phi'),\ \mathrm{asin}(\cos\lambda' \cos\phi') \,] \,. \tag{48}$$

It follows that the meridians of $G$ are connected to the parallels of $G'$ in the equatorial Atlantic — with equal tangents, but unequal curvatures. For $G$ and $G'$ to be compatible, it is obviously necessary that the grid sizes be such that $\Delta\lambda = \Delta\phi'$. It is also desirable, though not mandatory, that $\Delta\phi = \Delta\lambda'$. In the present model $\Delta\lambda = 3° = \Delta\phi$.

The "horizontal" coordinates $\tilde{x}$ and $\tilde{y}$ of the curvilinear coordinate system satisfy

$$\left(\frac{\partial}{\partial\tilde{x}}, \frac{\partial}{\partial\tilde{y}}\right) = \frac{1}{a}\left(\frac{\partial}{\partial\lambda}, \frac{\partial}{\partial\phi}\right) \text{ in } G \,, \tag{49}$$

$$\left(\frac{\partial}{\partial\tilde{x}}, \frac{\partial}{\partial\tilde{y}}\right) = \frac{1}{a}\left(\frac{\partial}{\partial\phi'}, -\frac{\partial}{\partial\lambda'}\right) \text{ in } G' \,. \tag{50}$$

The grid sizes are $\Delta\tilde{x} = a\,\Delta\lambda = a\,\Delta\phi'$ and $\Delta\tilde{y} = a\,\Delta\phi = a\,\Delta\lambda'$. As for the spherical coordinates used in most OGCMs, it is considered that the metric coefficients are such that $\partial h_x/\partial z = 0 = \partial h_y/\partial z$, and that $h_z = 1$. It follows that $(h_x, h_y) = (\cos\phi, 1)$ in $G$, and $= (1, \cos\phi')$ in $G'$.

Unlike $h_x$, the metric coefficient $h_y$ is discontinuous across the connection line of $G$ and $G'$: on the northern side of this line $h_y$ is equal to $\cos\phi'$, whereas it is equal to 1 in the Southern Hemisphere. If analytic calculations were carried out, this difficulty would be dealt with by simply matching the values of the dependent variables and the appropriate fluxes across the connection line. For the purposes of numerical calculations, a single value of $h_y$ is obviously required at $\phi = 0$. Consider a grid box straddling the Equator. Its area is about $a^2\,\Delta\lambda\,(\Delta\phi + \cos\phi'\,\Delta\lambda')/2$, which must be equivalent to $h_x\,h_y\,\Delta\tilde{x}\,\Delta\tilde{y}$. Hence, on the connection line, we must have

$$h_y = \frac{1 + \cos\phi'}{2} \,. \tag{51}$$

The model results will be pictured in the curvilinear coordinate system, in which equivalent latitude and longitude may be defined as $(\tilde{\lambda}, \tilde{\phi}) = a^{-1}\,(\tilde{x}, \tilde{y})$.

For simplicity, the wiggle "~" identifying the curvilinear coordinates will be dropped. For example, "$x$" will, in fact, mean "$\tilde{x}$".

It is easily seen that the two coordinate systems, associated with $G$ and $G'$, do not joint appropriately in the region of the Bering Strait. There is thus two options. First, we may consider the Bering Strait as closed, so that the lack of matching of $G$ and $G'$ does not matter. Second, according to Reason and Power (1994), the influence on the World Ocean general circulation of the Bering Strait flow, though small, may be regarded as non negligible, requiring that a method for allowing a northward water flux be worked out.

We opt for the second solution. However, no attempt is made to solve the governing equations of the model in the region of the strait. Instead, we parameterize the water, temperature and salinity fluxes crossing the Bering Strait, while the momentum flux is assumed negligible. Accordingly, an artificial water sink is placed in the Pacific grid boxes bordering on the Bering Shelf. A source of equal strength is located on the northern side of the strait. The water flux is proportional to the sea level difference between the Pacific and the Arctic grid boxes, in accordance with the hypothesis that this flow is geostrophically controlled (Overland

and Roach, 1987). A corresponding temperature and salinity flux is also prescribed. The parameterizations are tuned so that the northward water flow be of order $10^6$ m$^3$ s$^{-1}$.

**The meridional streamfunction.** It is not easy to understand the results of an OGCM, because of the complexity of the phenomena taking place in the World Ocean, and because of the large amount of real numbers generated by an OGCM. An example of an interpretation technique based on little graphical skill but considerable physical skill is the meridional streamfunction approach. This technique, which has now become a standard for visualising and discussing the results of OGCMs (*e.g.* Bryan 1982, 1987; Toggweiler *et al.*, 1989; Killworth *et al.*, 1991; Marotzke and Willebrand, 1991; England 1992; Semtner and Chervin, 1992) since it allows visualizing the "conveyor belt" circulation — which is described below. It consists in integrating the velocity in meridional planes over the longitudinal width of the ocean basin under study. Assuming that there is no water flux across the land and sea boundaries, the resulting two-dimensional vector field is divergenceless, implying that it may be represented with the help of a streamfunction, termed "meridional streamfunction" since the longitudinal velocity component is ignored. Contours of the streamfunction are drawn, and the difference between the streamfunction values associated with two given isolines corresponds to the water flux flowing between these isolines.

Assume that the domain of interest is defined as

$$[x_-(y), y_-, -h(x,y)] \;\le\; (x,y,z) \;\le\; [x_+(y), y_+, 0]\,, \tag{52}$$

where, for simplicity, the ocean surface is assumed flat ($\eta = 0$); $y_-$ and $y_+$ are constants. The two components of the transport that we want to represent are

$$(U, W) \;=\; \int_{x_-(y)}^{x_+(y)} (h_x v, h_x h_y w)\, dx\,. \tag{53}$$

The lateral boundaries of the domain of interest, located at $x_-(y)$ and $x_+(y)$, are either impermeable or periodic — if $x_-(y)$ corresponds to the same location of the terrestrial sphere as $x_+(y)$.

The continuity equation

$$\frac{\partial}{\partial x}(h_y u) + \frac{\partial}{\partial y}(h_x v) + \frac{\partial}{\partial z}(h_x h_y w) \;=\; 0\,, \tag{54}$$

is integrated over $x$, from $x_-(y)$ to $x_+(y)$, and, taking into account the lateral boundary conditions, it may be seen that

$$\frac{\partial V}{\partial y} + \frac{\partial W}{\partial z} \;=\; 0\,. \tag{55}$$

The transport $(V, W)$ is defined in the domain

$$[y_-, -d(y)] \;\le\; (y, z) \;\le\; [y_+, 0]\,, \tag{56}$$

where the depth $d$ is given by

$$d(y) \;=\; \max_{x_- \le x \le x_+} h(x,y)\,. \tag{57}$$



The domain defined in (56) has impermeable lower and upper boundaries, requiring that

$$[W(y,-d), W(y,0)] \;=\; [-V(y,-d)\frac{dd(y)}{dy}, 0]\,. \tag{58}$$

As indicated by (55), the transport $(V, W)$ is divergenceless, so that it may be represented with the help of a streamfunction, $\Psi$, as follows

$$(V, W) \;=\; [-\frac{\partial \Psi}{\partial z}, \frac{\partial \Psi}{\partial y}]\,. \tag{59}$$

The impermeability conditions (58) imply that $\Psi$ must be constant at the surface and the bottom of the domain of interest, *i.e.*,

$$[\Psi(y,-d), \Psi(y,0)] \;=\; (\Psi^b, \Psi^s) \tag{60}$$

where $\Psi^b$ and $\Psi^s$ are constants which denote the value of the streamfunction at the bottom and the surface, respectively. The difference $\Psi^b - \Psi^s$ is the — constant — water flux crossing the domain from $y_-$ to $y_+$.

**The surface boundary conditions.** The general circulation in the World Ocean is ultimately driven by the boundary conditions applied at the atmosphere-ocean interface on the momentum, the potential temperature and the salinity.

The wind stress, taken from the data set of Hellerman and Rosenstein (1983), is imposed at the sea surface as

$$[\rho K_u \frac{\partial \mathbf{u}}{\partial z}]_{\text{surface}} \;=\; \tau^s\,. \tag{61}$$

According to a frequently used ad hoc approach, the surface potential temperature, $T^s$, and salinity, $S^s$, are relaxed to their observed values through the following surface fluxes

$$[K_T \frac{\partial T}{\partial z}]_{\text{surface}} \;=\; -\frac{\Delta z^s}{T_r}(T^s - T^s_{\text{obs}})\,, \tag{62}$$

$$[K_S \frac{\partial S}{\partial z}]_{\text{surface}} \;=\; -\frac{\Delta z^s}{T_r}(S^s - S^s_{\text{obs}})\,, \tag{63}$$

where $\Delta z^s$ and $T_r$ respectively denote the height of the grid box adjacent to the ocean surface and the relaxation time scale, commonly taken to be equal to a few days to a few months; $T^s$ and $S^s$ represent the modelled surface temperature and salinity respectively, while $T^s_{\text{obs}}$ and $S^s_{\text{obs}}$ are their observed counterparts, obtained from the Levitus (1982) data set. The way conditions (62) and (63) work is easily understood. For example, if $T^s$ is larger than $T^s_{\text{obs}}$, the observed value, then the surface flux of temperature is upward, tending to decrease the surface temperature. Conversely, if $T^s < T^s_{\text{obs}}$, a downward temperature flux is prescribed at the sea surface.

Resorting to formulae (62)-(63) has some advantages. First, the boundary conditions do not require the knowledge of the surface fluxes, the observed values of which are generally poor. Second, as pointed out by Haidvogel and Bryan (1982), "it allows the model to develop structures and small-scale features not present in the forcing data", which are generally quite smooth.

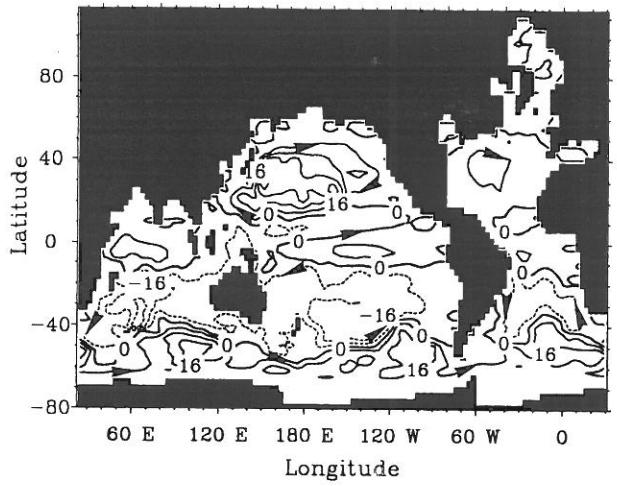


*Figure 13*. Barotropic streamfunction, $\Psi_b$, for run I (wind only simulation). The contour labels are in Sverdrups (1 Sv = $10^6$ m$^3$ s$^{-1}$). The arrows indicate the sense of circulation.

Boundary conditions (62)-(63) present, however, serious drawbacks. If the observed surface value is time-dependent, the variations of the modelled variable are likely to be smaller than those of the observed values, and there will probably be a phase lag. This may be understood by considering a simple equation for a given variable $\psi$,

$$\frac{\partial \psi}{\partial t} + u \frac{\partial \psi}{\partial x} = -\gamma(\psi - \psi_{obs}), \tag{64}$$

where $\gamma^{-1}$ and $u$ are an appropriate time scale and a constant advective velocity, respectively. We study Fourier components of the form

$$(\psi, \psi_{obs}) = \mathrm{Re}\{ (Y, Y_{obs}) \exp[I(\omega t - kx)] \}, \tag{65}$$

where $\omega$ and $k$ denote the angular frequency and the wavenumber, respectively. Introducing (65) into (64), we have

$$|Y| = \frac{1}{[1 + (\omega - uk)^2/\gamma^2]^{1/2}} |Y_{obs}|, \tag{66}$$

$$\arg Y = \arg Y_{obs} - \mathrm{atan}\frac{\omega - uk}{\gamma}, \tag{67}$$



which shows that the amplitude of $Y$ is smaller, in any case, than that of $Y_{obs}$. In addition, the phase lag — which may turn out to be negative — increases as $(\omega - uk)/\gamma$ increases. In the limit $(\omega - uk)/\gamma \to \infty$, the phase lag is $\pi/2$.

In the complete evolution equation for the potential temperature or the salinity, if the modelled surface value is equal to the observed one, then the modelled air-sea flux is zero, which is unlikely to be correct. Conversely, if the modelled air-sea flux is right — and non zero —, the modelled surface variable cannot be equal to its observed counterpart.

**The simulations.** As stated above, the circulation in the World Ocean is due to the wind and the thermohaline (*i.e.*, thermal and water fluxes at the air-sea interface) forcings. In an attempt to distinguish the respective roles of theses forcings, several numerical experiments are carried out with our OGCM.

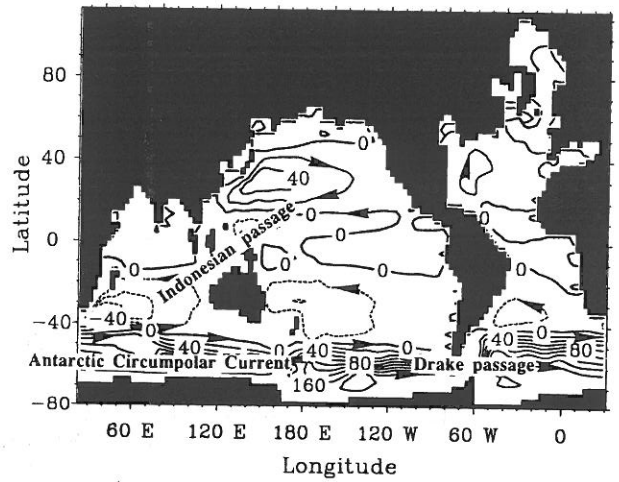


*Figure 14*. Barotropic streamfunction, $\Psi_b$, for run III (all the forcings with their seasonal cycle). The contour labels are in Sverdrups. The arrows indicate the direction of the circulation.

In the first run — hereafter referred to as I —, only the wind forcing is taken into account. Since the thermohaline forcing is neglected, the density of the water is considered constant, so that the horizontal pressure gradient force is depth-independent and is due to the slope of the ocean surface only. The seasonal cycle of the wind stress is implemented.

In the second simulation — hereafter II —, the annual mean of the wind and thermohaline forcings are taken into account. In this case, no forcing is omited, although the seasonal cycle is neglected.

The seasonal cycle of the forcings is retained in the third simulation — hereafter III. Of course, it is this numerical experiment that is likely to perform best.

All model results presented below are yearly means, evaluated when the model has reached a well established regime, *i.e.*, when the transients associated with the initial conditions have become negligible.

*Table 5.* Flow (in Sverdrups) through the Drake passage (eastward) and the Indonesian passage (from Pacific to Indian); North Atlantic overturning (in Sverdrup) and North Atlantic Deep Water (NADW) flow toward the Southern Ocean at 20°S (in Sverdrups). The observed estimates are due to Nowlin and Klinck (1986) for the Drake passage, Godfrey (1989) for the Indonesian passage, Gordon (1986) and Hall and Bryden (1982) for the North Atlantic overturning, Gordon (1986) and Broecker (1991) for the southward NADW flow at 20°S. See also Figs. 13–17.

| | observed | I | II | III |
|---|---|---|---|---|
| Drake passage: | 120 – 150 | 13. | 134. | 168. |
| Indonesian passage: | O(12) | 8.4 | 15.1 | 15.6 |
| N. Atlantic overturning: | 15 – 20 | meaningless | 12.9 | 17.6 |
| NADW southward (20°S): | 13–20 | meaningless | 6.3 | 9.0 |

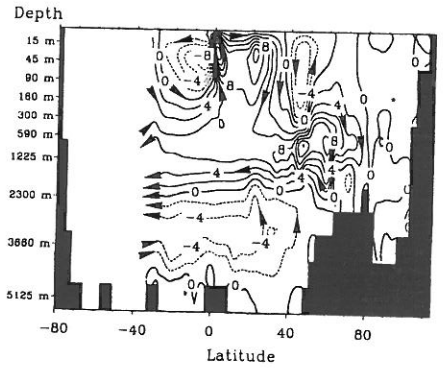


*Figure 15.* Meridional streamfunction, $\Psi$, in the Atlantic and Arctic for simulation II (all forcings without seasonal cycle). The contour labels are in Sverdrups. The arrows indicate the direction of the circulation.



First, we examine the barotropic streamfunction, $\Psi_b$, which is used to represent the horizontal transport according to

$$(-\frac{\partial \Psi_b}{\partial y}, \frac{\partial \Psi_b}{\partial x}) = \int_{-h}^{\eta} (h_y u, h_x v)\, dz\,. \tag{68}$$

As may be seen in Fig. 13, the pattern of $\Psi_b$ of run I is qualitatively similar to that of the hopefully more realistic simulation III. It must however be stressed that the Antarctic Circumpolar Current is almost absent from the wind-only simulation. The eastward flow through Drake passage is much weaker in I than in II or III (Table 5). Surprinsingly, the Drake passage transport is probably better when the seasonal cycle of the wind and thermohaline forcings is not taken into account (Table 5). In I, the large subtropical gyres are present, but exhibit weaker transports than in the experiment III (Fig. 14). The transport through the Indonesian passage is probably too small in I, and too large in II and III (Table 5). Overall, it is clear that the wind-only simulation exhibits large errors — especially in the representation of the Antarctic Circumpolar Current.

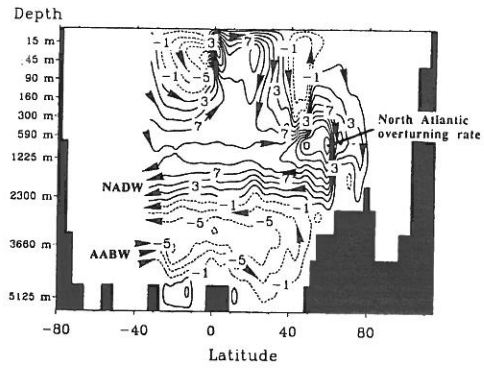


*Figure 16.* Meridional streamfunction, $\Psi$, in the Atlantic and Arctic for simulation III (all forcings with seasonal cycle). The contour labels are in Sverdrups. The arrows indicate the direction of the circulation.

The meridional circulation in the Atlantic is a key process for the circulation in the whole World Ocean. North Atlantic Deep Water (NADW) is formed by convective processes in the North Atlantic (Killworth, 1983). This cold and salty water mass flows southward, above a cell of Antarctic Bottom Water (AABW), formed by convective processes in the vicinity of the Antarctic continent. The southward flow of NADW is compensated by a shallow, warm current, flowing northward. This circulation scheme is qualitatively well represented in II (Fig. 15) and III (Fig. 16), but not at all in I (Fig. 17). The NADW is exported to the Indian and

Pacific Oceans through the Antarctic Circumpolar Current. In the Northern part of the Indian and Pacific Oceans, upwelling is taking place. Finally a warm, shallow water current returns to the Atlantic, through the Indonesian Passage, the Indian Ocean and a branch of the Agulhas Current — around the southern tip of Africa. This return route is usually called "warm water route", as opposed to the "cold water route" — Pacific to Atlantic through Drake Passage —, which is probably of lesser importance (Gordon, 1986; Doos, 1994). This global ocean circulation scheme is known as the "conveyor belt" (Gordon, 1986, Broecker, 1991).

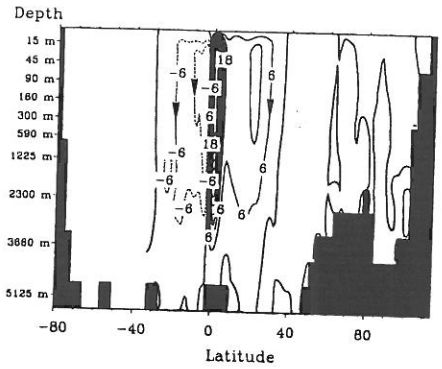


*Figure 17.* Meridional streamfunction, $\Psi$, in the Atlantic and Arctic for simulation I (wind-only simulation). The contour labels are in Sverdrups. The arrows indicate the direction of the circulation.

The North Atlantic overturning, roughly speaking the production rate of NADW, and the NADW southward transport, evaluated at 20°S, are significantly better in simulation III than in II, where the seasonal cycle of the forcing is absent (Table 5). The two equatorial upwelling cells are present in all numerical experiments, but those of run I reach a depth of about 4000 m, while the depth of those of the other simulations does not exceed 200–300 m, which is certainly more realistic.

From the model results discussed above, it seems clear that the wind forcing alone cannot account resonably well for the circulation in the World Ocean, which does not mean that the wind stress should be neglected. The wind only simulation fails to represent most important features of the circulation in both the horizontal and meridional planes.

As regards the simulations with wind and thermohaline forcings, the annual means of the circulation parameters examined in Table 5 are more realistic when the seasonal cycle of the forcings are taken into account.

As indicated in Table 6, the properties of the water masses are fairly well represented in simulation III, except that the thermocline and intermediate waters — located at depth ranging from 200 to 1200 m, say — are too warm. This deficiency may be due to the fact that the model is in general too diffusive and that no isopycnal diffusion scheme is activated.



*Table 6.* Difference between the modelled — in run III — water mass properties and the Levitus (1982) climatological values. The quantity $\Delta\psi$ denotes the average over the surface of the World Ocean of the modelled variable, *i.e.*, potential temperature (in °C) or salinity (in PSU), and the corresponding value in the Levitus (1982) climatology; $\Delta\psi_{rms}$ represent the root mean square difference. All statistical quantities are evaluated at the 20 model levels, the depths of which are given in meters.

| level | depth | $\Delta T$ | $\Delta T_{rms}$ | $\Delta S$ | $\Delta S_{rms}$ |
|---|---|---|---|---|---|
| 1 | 5 | –0.003 | 0.7 | 0.0003 | 0.1 |
| 2 | 16 | –0.4 | 1.1 | 0.002 | 0.2 |
| 3 | 29 | –0.5 | 1.5 | 0.002 | 0.3 |
| 4 | 45 | –0.3 | 1.6 | –0.02 | 0.4 |
| 5 | 65 | 0.1 | 1.7 | –0.03 | 0.4 |
| 6 | 90 | 0.5 | 1.9 | –0.05 | 0.4 |
| 7 | 122 | 0.9 | 2.1 | –0.06 | 0.4 |
| 8 | 163 | 1.0 | 2.1 | –0.05 | 0.3 |
| 9 | 219 | 1.6 | 2.4 | –0.02 | 0.3 |
| 10 | 299 | 2.0 | 2.7 | 0.03 | 0.3 |
| 11 | 415 | 2.6 | 3.1 | 0.1 | 0.3 |
| 12 | 589 | 2.9 | 3.4 | 0.1 | 0.3 |
| 13 | 850 | 3.0 | 3.3 | 0.07 | 0.3 |
| 14 | 1225 | 2.5 | 2.7 | –0.04 | 0.2 |
| 15 | 1718 | 1.6 | 1.7 | –0.2 | 0.2 |
| 16 | 2307 | 0.9 | 1.1 | –0.2 | 0.3 |
| 17 | 2963 | 0.6 | 0.7 | –0.3 | 0.3 |
| 18 | 3661 | 0.3 | 0.6 | –0.3 | 0.3 |
| 19 | 4385 | 0.1 | 0.5 | –0.4 | 0.4 |
| 20 | 5126 | 0.07 | 0.4 | –0.3 | 0.4 |

An important variable for global climate is the poleward heat transport, $p$. The latter is calculated from the model results as

$$p = \int_{-h}^{0} \int_{x_-}^{x_+} h_x v T \, dx \, dz \,, \tag{69}$$

where the interval $[x_-, x_+]$ spans the whole terrestrial sphere along a curve where $y$ is constant. In the Northern Hemisphere, this quantity is larger in III than in II (Fig. 18). In both hemispheres, the poleward heat transport is somewhat smaller than the estimates derived from observations (*e.g.* Hastenrath, 1982; Hsiung, 1985). This deficiency is common to many OGCMs (*e.g.* Semtner and Chervin, 1992; Maier-Reimer *et al.*, 1993). However, other recent numerical experiments have achieved quite realistic heat transports in the Southern Hemisphere (England, 1993; Hirst and Cai, 1994), as well as in the Northern Hemisphere (Hirst and Cai, 1994).

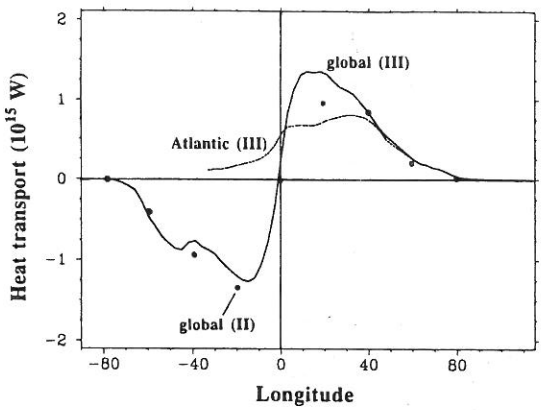


*Figure 18.* Poleward heat tranport (in $10^{15}$ Watts) in run III and in run II (dots) achieved by the World Ocean. For run III, the contribution of the Atlantic is also given (dotted curve).

## Appendix

A few ways of dealing with the external mode of an ocean model are outlined here.

Integrating the continuity equation over the whole water column, taking into account the impermeability conditions of the surface and the bottom, we obtain

$$\frac{\partial \eta}{\partial t} = -\nabla \cdot \mathbf{U} , \tag{A1}$$

where $\mathbf{U}$ is the horizontal transport, *i.e.*, the depth-integral of the horizontal velocity.

The depth-integral of the horizontal momentum equation may be written as

$$\frac{\partial \mathbf{U}}{\partial t} = -f \mathbf{e}_z \times \mathbf{U} - g H \nabla \eta + \mathbf{F} , \tag{A2}$$

where $\mathbf{F}$ encompasses many terms, the list of which does not need to be given here.

For simplicity, we have written equations (A1)-(A2) in the beta-plane: Earth's curvature is neglected — so that cartesian coordinates may be used —, except in the Coriolis factor. The latter is assumed to be a linear function of a space coordinate,

$$f = f_0 + \beta y , \tag{A3}$$

where $f_0$ and $\beta$ are constants. For the beta-plane approximation to be valid, it is necessary that the size of the domain of interest, characterized by length scale $L$, be much smaller than the Earth's radius. In addition, we must also have $\beta L << f_0$. Further details on the beta-plane theory are given in classical treatises of geophysical fluid dynamics (*e.g.* Cushman-Roisin, 1994).



Equations (A1)-(A2) are depth-independent, and are mainly concerned with motions associated with the slope of the ocean surface. This is the reason that the ocean phenomena obeying these equations are referred to as the "external mode", as opposed to the "internal mode", in which the slope of density surfaces is the main source of motion.

To grasp the dynamics of the external mode, as well as that of the internal mode, it is helpful to examine wavelike phenomena. It may be seen that the internal waves, *i.e.*, the waves of the internal mode, propagate at a phase speed that does not exceed a few meters per second. Note in passing that this velocity is of the same order of magnitude as that of the fastest advective processes. On the other hand, the external mode can sustain waves propagating as fast as several hundreds of meters per second. Now, most numerical stability criteria are of the form

$$\Delta t \leq \frac{\Delta x}{c_p} , \tag{A4}$$

where $c_p$ is the fastets propagation speed of the phenomena considered. Therefore, the time step of the numerical algorithm will be constrained by the external mode processes.

If the fast external waves could be ignored, the allowable time step would be 10 – 100 times larger. This situation is so frustrating that several methods for circumventing the external wave constraint, and hence for speeding up ocean models, have been suggested. However, before outlining some of them, it is worth investigating the wave phenomena associated with the external mode.

Equations (A1)-(A2) may be simplified and linearized to

$$\chi \frac{\partial \eta}{\partial t} + \frac{\partial U}{\partial x} + \frac{\partial V}{\partial y} = 0 , \tag{A5}$$

$$\frac{\partial U}{\partial t} - f V = -g h \frac{\partial \eta}{\partial x} , \tag{A6}$$

$$\frac{\partial V}{\partial t} + f U = -g h \frac{\partial \eta}{\partial y} , \tag{A7}$$

where $h$, $U$ and $V$ denote the ocean depth — assumed constant — and the two components of the transport, respectively. Of course, (A5)-(A7) are formally equivalent to (8)-(10), except that, in the latter, the Coriolis factor is considered as constant — as it should be in the $f$-plane approximation. In (A5), the coefficient $\chi$ is normally equal to 1, but may be set to 0 when the "rigid lid" approximation is introduced, as will be done below.

Appropriate manipulations of (A5)-(A7) lead to (Longuet-Higgins, 1965)

$$\frac{\chi}{g h} \left( \frac{\partial^2}{\partial t^2} + f^2 \right) \frac{\partial V}{\partial t} = \nabla^2 \frac{\partial V}{\partial t} + \beta \frac{\partial V}{\partial x} . \tag{A8}$$

Since $\beta y << f_0$, we may consider that $f = f_0$ in the equation above. The latter then has constant coefficient, so that plane wave solutions may be sought. For this solution, let $\omega$, $k_x$ and $k_y$ represent the angular frequency, and the wavenumbers in both space directions. The dispersion relation of the waves under study reads

$$\frac{\alpha}{g h} (\omega^2 - f_0^2) \omega = (k_x^2 + k_y^2) \omega + \beta k_x . \tag{A9}$$

If the ocean surface is regarded as a "free-surface", *i.e.*, if $\chi = 1$, (A9) admits two classes of wave processes. The fast processes, the Poincaré waves (see also Section 3), for which $|\omega| >> \beta\,|k_x| / (k_x^2 + k_y^2)$, are such that

$$\omega = \pm [\, f_0^2 + g\,h\,(k_x^2 + k_y^2)\,]^{1/2} . \tag{A10}$$

These waves are — asymptotically — not affected by the Earth's curvature, since (A10) does not encompasses $\beta$. The slow processes contained in (A9) emerge when small angular frequencies are considered, *i.e.*, $\omega^2 << f_0^2$. The corresponding wave processes, called "planetary waves" or "Rossby waves", obey the following dispersion relation

$$\omega = \frac{-\,g\,h\,\beta\,k_x}{f_0^2 + g\,h\,(k_x^2 + k_y^2)} . \tag{A11}$$

The phase speed of the Poincaré and Rossby waves are displayed in Fig. A1 — in a non-asymptotic form.

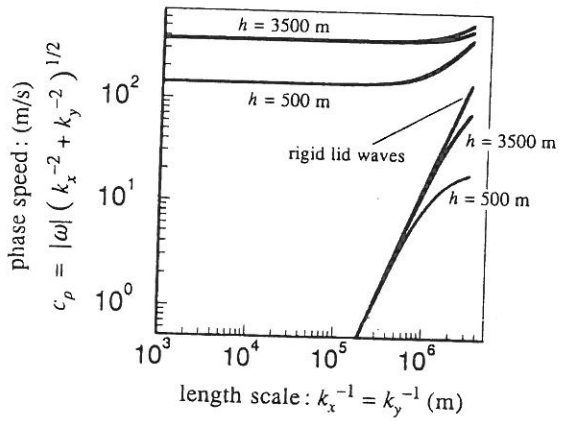


*Figure A1*. Phase speed of the waves characterized by dispersion relation (A9) (free surface) and by (A13) (rigid lid) for an ocean depth of $h$ = 3500 m and $h$ = 500 m. We have taken $f_0 = 8\text{x}10^{-5}$ s$^{-1}$ and $\beta = 2\text{x}10^{-11}$ m$^{-1}$ s$^{-1}$, *i.e.*, typical mid-latitudes values.

It is far from clear that fast processes, such as the Poincaré waves, need to be included into a climate models — since climate is presumably determined by much slower phenomena. In the World Ocean, the fast external waves contain a very small amount of the total energy (*e.g.* Zhang and Endoh, 1992). In a climate model, it is thus tempting to ignore these processes. An elegant way of filtering them out is to drop the time-derivative of $\eta$ in (A1), which thus transforms to



$$\nabla \bullet \mathbf{U} = 0 . \tag{A12}$$

This is the "rigid lid" approximation. In the linearized study, this amounts to setting $\chi = 0$, so that dispersion relation (A9) reduces to

$$\omega = \frac{-\,\beta\,k_x}{k_x^2 + k_y^2} . \tag{A13}$$

In other words, by resorting to the rigid lid appoximation, the Poincaré waves are excluded, and only modified Rossby waves, *i.e.*, slow processes, are possible. It is easily seen that (A13) is asymptotic to (A11), when $(k_x^2 + k_y^2)^{-1/2} << (g\,h)^{1/2}/f_0$, *i.e.*, when the length scale of the phenomena under study is much smaller than the external Rossby radius of deformation, $(g\,h)^{1/2}/f_0$.

As may be seen in Fig. A1, the phase speeds of rigid lid and free surface Rossby waves are almost equal, except for the longest waves, for which significant discrepancies may be found.

In shallow sea models, the external mode, *i.e.*, essentially the tides and storm surges, usually contains much of the kinetic energy. In this case, making the rigid lid approximation is out of the question.

In deep-sea or ocean modelling, the tradition has been to resort to the rigid lid approximation. Bryan (1969) decided to represent the transport by means of a barotropic streamfunction, defined as in (68), in order for the continuity equation (A12) to be identically satisfied. Dividing (A2) by the ocean depth, taking the curl of the resulting relation to eliminate the gradient of $\eta$, using the streamfunction representation, we obtain

$$\nabla \bullet [\, h^{-1}\, \nabla \frac{\partial \Psi_b}{\partial t} \,] = \mathbf{e}_z \bullet [\, \nabla \times h^{-1}\, (-f\,\mathbf{e}_z \times \mathbf{U} + \mathbf{F}\,)\,] \tag{A14}$$

The streamfunction is prescribed to be constant along the coastlines limiting the computational domain to enforce the impermeability of these boundaries. When discretized in time, (A14) may be regarded as a Poisson equation for $\Psi_b$ at the new time level. This approach may present several problems. Killworth and Smith (1984) pointed to possible instabilities in the iterative procedure classically used to solve (A14). Furthermore, the $h^{-1}$ coefficient appearing in the left-hand side of (A14) was also shown to be detrimental to the numerical method (Dukowicz *et al.*, 1993). Finally, the nature of the boundary condition applied at the coastline of islands implies the evaluation of non-local integrals, leading to data transfers that can seriously reduce the performance of modern distributed memory computers (Dukowicz *et al.*, 1993).

If the divergence of the momentum equation (A2) is taken, rather than the curl, a Poisson equation for the ocean surface elevation is obtained:

$$\nabla \bullet (g\,h\,\nabla \eta) = -\,\nabla \bullet (f\,\mathbf{e}_z \times \mathbf{U}) + \nabla \bullet \mathbf{F} . \tag{A15}$$

In the framework of the rigid approximation, the ocean surface elevation may be considered a linear function of the "pressure acting on the rigid lid placed at the reference level of the ocean surface" (*e.g.* Deleersnijder, 1994b; Pinardi *et al.*, 1995). From a numerical point of view, (A15) is better conditioned than (A14): steep bottom slopes are more easily taken into account and the impermeability boundary conditions involve local computations only (Gresho and Sani, 1987; Deleersnijder and Campin, 1993; Dukowicz *et al.*, 1993; Pinardi *et al.*, 1995). If n

denotes the unit vector normal to the coastline, the impermeability condition $\mathbf{U}\bullet\mathbf{n} = 0$, when applied to (A2), leads to

$$g\,h\,\nabla\eta\bullet\mathbf{n} \;=\; (-f\,\mathbf{e}_z \times \mathbf{U} + \mathbf{F})\bullet\mathbf{n}\,, \tag{A16}$$

which is indeed a purely local boundary condition for $\eta$.

The alternative to the rigid lid approximation is to consider the ocean surface as free. As a result, $\eta$ is a prognostic variable of the model, *i.e.*, a variable that may be computed from an evolution equation, namely (A1). This could allow studying phenomena such as tides or the inverted barometer effect (Ponte, 1993). To overcome the severe limitations of the time step due to the presence of fast-propagating Poincaré waves, the split-explicit method (Gadd, 1978; Madala, 1981) may be used, as is done in our OGCM, as well as in other models (Blumberg and Mellor, 1987; Beckers, 1991; Killworth *et al.*, 1991). The split explicit technique consists in integrating the external and internal modes — according to a mainly explicit time stepping — with different time steps, each time increment being selected according to the fastest-propagating phenomenon encountered in the mode considered. Even though the external time step is 10–100 times smaller than that of the internal mode, the treatment of the external mode generally requires 10% of the total computer cost, because the external mode equations are two-dimensional, and thus much cheaper to deal with than the internal mode, which is three-dimensional. A recent variant of the free-surface approach is to integrate the external mode equations by means of a semi-implicit method, allowing a much longer time step to be used (Casulli and Cheng, 1992; Casulli and Catani, 1994; Dukowicz and Smith, 1994).

It is conceivable that, in the future, the streamfunction approach will cease to be the favourite option. Whether or not all models will switch to the free surface formulation is far from clear. It is however worth stressing that Dukowicz and Smith (1994), in the scope of their eddy-resolving World Ocean model, identified no less than 6 advantages of the implicit free surface solution method.

## References


Adam, P. (1990) *Modélisation Mathématique Tridimensionnelle d'un Ecosystème Marin – Application à la Région du Détroit de Bering*, Mémoire de Fin d'Etudes, Faculté des Sciences Appliquées, Université de Liège, 159 pp.

Arakawa, A. and Lamb, V.R. (1977) Computational design of the basic dynamical processes of the UCLA general circulation model, *Methods in Computational Physics*, Vol. 17, Academic Press, 337 pp.

Batteen, M.L. and Han, Y.-J. (1981) On the computational noise of finite-difference schemes used in ocean models, *Tellus*, 33, 387–396.

Beckers, J.-M. (1991) Application of the GHER 3D general circulation model to the Western Mediterranean, *J. Mar. Syst.*, 1, 315–332.

Beckers, J.-M. (1992) Analytical linear numerical stability conditions for an anisotropic 3D advection-diffusion equation, *SIAM J. Numer. Anal.*, 29, 701–713.

Beckers, J.-M. and Deleersnijder, E. (1993) Stability of a FBTCS scheme applied to the propagation of shallow-water inertia-gravity waves on various space grids, *J. Comput. Phys.*, 108, 95–104.

Bedford, K.W. Dingman, J.S. and Yeo, W.K. (1987) Preparation of estuary and marine model equations by generalized filtering methods, *Three-Dimensional Models of Marine and Estuarine Dynamics* (J.C.J. Nihoul and B.M. Jamart, Editors), Elsevier, pp. 113–125.

Bennett, A.F. (1992) *Inverse Methods in Physical Oceanography*, Cambridge Univ. Press, 346 pp.





Blumberg, A.F. and Mellor, G.L. (1987) A description of a three-dimensional coastal ocean circulation model, *Three-Dimensional Coastal Ocean Models* (N.S. Heaps, Editor), American Geophysical Union, pp. 1–16.

Blumen, W. (1972) Geostrophic adjustment, *Rev. Geophys. and Space Phys.*, 10, 485–528.

Boussinesq, J. (1877) Essai sur la théorie des eaux courantes, *Mém. Acad. Sci. Paris*, 23, 1–680.

Brasseur, P.P. (1991) A variational inverse method for the reconstruction of general circulation fields in the Northern Bering Sea, *J. Geophys. Res.*, 96, 4891–4907.

Brasseur, P.P. and Haus, J. (1991) Application of a 3-D variational inverse model to the analysis of ecohydrodynamic data in the Northern Bering and Southern Chukchi seas, *J. Mar. Syst.*, 1, 383–401.

Broecker, W.S. (1991) The great ocean conveyor, *Oceanogr.*, 4, 79–89.

Bryan, K. (1969) A numerical method for the study of the circulation of the World Ocean, *J. Comput. Phys.*, 4, 347–376.

Bryan, K. (1982) Seasonal variation in meridional overturning and poleward heat transport in the Atlantic and Pacific oceans, *J. Mar. Res.*, 40, 39–53.

Bryan, K. (1987) Parameter sensitivity of primitive equations ocean general circulation models, *J. Phys. Oceanogr.*, 17, 970–985.

Casulli, V. and Cattani, E. (1994) Stability, accuracy and efficiency of a semi-implicit method for three-dimensional shallow water flow, *Computers Math. Applic.*, 27, 99–112

Casulli, V. and Cheng, R.T. (1992) Semi-implicit finite difference methods for three-dimensional shallow water flow, *Int. J. Numer. Methods Fluids*, 15, 629–648.

Coachman, L.K. and Aagaard, K (1966) On the water exchange through Bering Strait, *Limnol. Oceanogr.*, 11, 44–59.

Coachman, L.K. and Aagaard, K (1988) Transports through Bering Strait: annual and interannual variability, *J. Geophys. Res.*, 93, 15535–15539.

Coachman, L.K., Aagaard, K. and Tripp, R.B. (1975) *Bering Strait – The Regional Physical Oceanography*, Univ. of Washington Press, 172 pp.

Coward, A.C., Killworth, P.D. and Blundell, J.R. (1995) Tests of a two-grid world ocean model, *J. Geophys. Res.* (in press).

Cox, M. (1984) *A Primitive Equation, Three-Dimensional Model of the Ocean*, GFDL Ocean Group, Tech. Rep. No. 1, GFDL/NOAA, Princeton.

Cushman-Roisin, B. (1984) Analytical, linear stability criteria for the leap-frog, Dufort-Frankel method, *J. Comput. Phys.*, 53, 227–239.

Cushman-Roisin, B. (1994) *Introduction to Geophysical Fluid Dynamics*, Prentice Hall, 320 pp.

Deleersnijder, E. (1989) Upwelling and upsloping in three-dimensional marine models, *Appl. Math. Model.*, 13, 462–467.

Deleersnijder, E. (1992) *Modélisation Hydrodynamique Tridimensionnelle de la Circulation Générale Estivale de la Région du Détroit de Bering*, Thèse de Doctorat, Faculté des Sciences Appliquées, Université Catholique de Louvain, 189 pp.

Deleersnijder, E. (1994a) An analysis of the vertical velocity field computed by a three-dimensional model in the region of the Bering Strait, *Tellus*, 46A, 134–148.

Deleersnijder, E. (1994b) The assimilation of altimetric data into the barotropic mode of a rigid lid ocean model, *Mathl. Comput. Modelling*, 20, 85–94.

Deleersnijder, E. and Campin, J.-M. (1993) *Du Calcul de la Position de la Surface de l'Océan dans un Modèle de Circulation Générale*, Contribution no. 70, Institut d'Astronomie et de Géophysique G. Lemaître, Université Catholique de Louvain, Louvain-la-Neuve.

Deleersnijder, E. and Campin, J.-M. (1995) On the computation of the barotropic mode of a free-surface World Ocean model, *Ann. Geophys.* (in press).

Deleersnijder, E. and Luyten, P. (1994) On the practical advantages of the quasi-equilibrium version of the Mellor and Yamada level 2.5 turbulence closure applied to marine modelling, *Appl. Math. Model.*, 18, 281–287.

Deleersnijder, E. and Wolanski, E. (1990) Du rôle de la dispersion horizontale de quantité de mouvement dans les modèles marins tridimensionnels, *Journées Numériques de Besançon 1990 — Courants Marins* (J.-M. Crolet and P. Lesaint, Editors), Publications Mathématiques de Besançon, pp. 39–50.

Deleersnijder, E., van Ypersele, J.-P., and Campin, J.-M. (1993) An orthogonal curvilinear coordinate system for a World Ocean model, *Ocean Modelling*, 100, 7–10 (+ figs.).
Doos, K. (1994) Inter-ocean exchange of water masses (submitted).
Dukowicz, J.K. and Smith, R.D. (1994) Impicit free-surface method for the Bryan-Cox-Semtner ocean model, *J. Geophys. Res.*, 99, 7991–8014.
Dukowicz, J.K., Smith, R.D. and Malone, R.C. (1993) A reformulation and implementation of the Bryan-Cox-Semtner ocean model on the Connection Machine, *J. Atmos. Ocean. Technol.*, 10, 195–208.
Eby M. and Holloway, G. (1994) Grid transformation for incorporating the Arctic in a global ocean model, *Clim. Dyn.*, 10, 241–247.
England, M.H. (1992) On the formation of Antarctic Intermediate and Bottom Water in ocean general circulation models, *J. Phys. Oceanogr.*, 22, 918–926.
England, M.H. (1993) Representing the global-scale water masses in ocean general circulation models, *J. Phys. Oceanogr.*, 23, 1523–1552.
Gadd, A.J. (1978) A split-explicit integration scheme for numerical weather prediction, *Q. J. R. Meteorol. Soc.*, 104, 569–582.
Galperin, B., Kantha, L.H., Hassid, S. and Rosati, A. (1988) A quasi-equilibrium turbulent energy model for geophysical flows, *J. Atmos. Sci.*, 45, 55–62.
Godfrey, A.L. (1989) A Sverdrup model of the depth-integrated flow for the World Ocean allowing for island circulations, *Geophys. Astrophys. Fluid Dyn.*, 45, 89–112.
Gordon, A.L. (1986) Interocean exchange of thermocline water, *J. Geophys. Res.*, 91, 5037–5046.
Gresho, P.M. and Sani, R.L. (1987) On pressure boundary conditions for the incompressible Navier-Stokes equations, *Int. J. Numer. Methods Fluids*, 7, 1111–1145.
Haidvogel, D.B. and Bryan, F.O. (1992) Ocean general circulation modeling, *Climate System Modeling* (K.E. Trenberth, Editor), Cambridge University Press, pp. 371–412.
Hall M.M. and Bryden, H.L. (1982) Direct estimates and mechanisms of ocean heat transport, *Deep-Sea Res.*, 29, 339–359.
Hastenrath, S. (1982) On meridional heat transports in the World Ocean, *J. Phys. Oceanogr.*, 12, 922–927.
Helfand, H.M. and Labraga, J.C. (1988) Design of a nonsingular level 2.5 second-order closure scheme for the prediction of atmospheric turbulence, *J. Atmos. Sci.*, 45, 113–132.
Hellerman, S. and Rosenstein, M. (1983) Normal monthly wind stress over the world ocean with error estimates, *J. Phys. Oceanogr.*, 13, 1093–1104.
Hirsch, C. (1988) *Numerical Computation of Internal and External Flows. Vol. 1: Fundamentals of Numerical Discretization*, Wiley, 515 pp.
Hirst, A.C. and Cai, W. (1994) Sensitivity of a World Ocean GCM to changes in subsurface mixing parameterization, *J. Phys. Oceanogr.*, 24, 1256–1279.
Houghton, J.T., Callander, B.A. and Varney, S.K. (Editors) (1992) *Climate Change 1992: The Supplement Report to the IPCC Scientific Assessment*, Cambridge University Press, 200 pp.
Houghton, J.T., Jenkins, G.J. and Ephraums, J. (Editors) (1990) *Climate Change: The IPCC Scientific Assessment*, Cambridge University Press, 364 pp.
Hsiung, J. (1985) Estimates of global oceanic meridional heat transport, *J. Phys. Oceanogr.*, 15, 1405–1413.
Kato, H. and Phillips, O.M. (1969) On the penetration of a turbulent layer into stratified fluid, *J. Fluid Mech.*, 37, 643–655.
Killworth, P.D. (1983) Deep convection in the worl ocean, *Rev. Geophys.*, 21, 1–26.
Killworth, P.D. and Smith, J.M. (1984) Gradual instability of relaxation-extrapolation scheme, *Dyn. Atmos. Oceans*, 8, 185–213.
Killworth, P.D., Stainforth, D., Webb, D.J. and Paterson, S.M. (1991) The development of a free-surface Bryan-Cox-Semtner ocean model, *J. Phys. Oceanogr.*, 21, 1333–1348.
LeBlond, P.H. and Mysak, L.A. (1978) *Waves in the Ocean*, Elsevier, 602 pp.
Levitus, S. (1982) *Climatological Atlas of the World Oceans*, NOAA Prof. Paper 13, U.S. Gov. Print. Office, Washington, D.C.
Longuet-Higgins, M.S. (1965) Planetary waves on a rotating sphere, II, *Proc. R. Soc. London*, 284A, 40–68.



Luyten, P., Deleersnijder, E., Ozer, J. and Ruddick, K. (1994) Presentation of a family of turbulence closure models for stratified shallow water flows and preliminary application to the Rhine outflow region, *Cont. Shelf Res.* (in press).
Madala, R.V. (1981) Efficient time integration schemes for atmosphere and ocean models, *Finite-Difference Techniques for Vectorized Fluid Dynamics Calculations* (D.L. Book, Editor), Springer-Verlag, pp. 56–74.
Maier-Reimer, E., Mikolajewicz, U. and Hasselmann, K. (1993) Mean circulation of the Hamburg LSG OGCM and its sensitivity to the thermohaline surface forcing, *J. Phys. Oceanogr.*, 23, 731–757.
Marotzke, J. and Willebrand, J. (1991) Multiple equilibria of the global thermohaline circulation, *J. Phys. Oceanogr.*, 21, 1372–1385.
Marti, O., Chartier, M. and Delecluse, P. (1990) A World Ocean model in curvilinear coordinates, *Journées Numériques de Besançon 1990 — Courants Marins* (J.-M. Crolet and P. Lesaint, Editors), Publications Mathématiques de Besançon, pp. 17–25.
Marti, O., Madec, G. and Delecluse, P. (1992) Comments on "Net diffusivity in ocean general circulation models with nonuniform grids" by F.L. Yin and I.Y. Fung, *J. Geophys. Res.*, 97, 12763–12766.
Mellor, G.L. and Blumberg, A.F. (1985) Modeling vertical and horizontal diffusivities with the sigma coordinate system, *Mon. Weather Rev.*, 113, 1379–1383.
Mellor, G.L. and Strub, P.T. (1980) Similarity solutions for the stratified turbulent Rayleigh problem, *J. Phys. Oceanogr.*, 10, 455–460.
Mellor, G.L. and Yamada, T. (1982) Development of a turbulence closure model for geophysical fluid problems, *Rev. Geophys. and Space Phys.*, 20, 851–875.
Mesinger, F. and Arakawa, A. (1976) *Numerical Methods Used in Atmospheric Models*, GARP Publications Series (no. 17, vol. 1), WMO-ICSU Joint Organizing Committee, 64 pp.
Monin, A.S. (1975) The role of the oceans in climate models, *The Physical Basis of Climate and Climate Modelling* (no. 16, Appendix 6), WMO-ICSU Joint Organizing Committee, pp. 201–205.
Nihoul, J.C.J. (1994) Do not use a simple model when a complex one will do, *J. Mar. Syst.*, 5, 401–406.
Nihoul, J.C.J., Adam, P., Brasseur, P., Deleersnijder, E., Djenidi, S. and Haus, J. (1993a) Three-dimensional general circulation model of the northern Bering Sea's summer ecohydrodynamics, *Cont. Shelf Res.*, 13, 509–542.
Nihoul, J.C.J., Adam, P., Djenidi, S. and Deleersnijder, E. (1993b) Modelling the coastal ocean's complex ecohydrodynamics – A case study: the Northern Bering Sea, *Progress in Belgian Oceanographic Research*, Royal Academy of Belgium, pp. 203–216.
Nihoul, J.C.J. and Djenidi, S. (1987) Perspective in three-dimensional modelling of the marine system, *Three-Dimensional Models of Marine and Estuarine Dynamics* (J.C.J. Nihoul and B.M. Jamart, Editors), Elsevier, pp. 1–33.
Niiler, P.P. (1992) The ocean circulation, *Climate System Modeling* (K.E. Trenberth, Editor), Cambridge University Press, pp. 117–148.
Nowlin, W.D. and Klinck, J.M. (1986) The physics of the Antarctic circumpolar current, *Rev. Geophys.*, 24, 469–491.
Overland, J.E. and Roach, A.T. (1987) Northward flow in the Bering and Chukchi Seas, *J. Geophys. Res.*, 92, 7097–7105.
Pacanowski, R.C. and Philander, S.G.H. (1981) Parameterization of vertical mixing in numerical models of tropical oceans, *J. Phys. Oceanogr.*, 11, 1443–1451.
Patankar, S.V. (1980) *Numerical Heat Transfer and Fluid Flow*, Hemisphere, 197 pp.
Peyret, R. and Taylor, T.D. (1983) *Computational Methods for Fluid Flow*, Springer-Verlag, 358 pp.
Phillips, N.A. (1957) A coordinate system having some special advantages for numerical forecasting, *J. Meteorol.*, 14, 184–185.
Pinardi, N., Rosati, A. and Pacanowski, R.C. (1995) The sea surface pressure formulation of rigid lid models. Implications for altimetric data assimilation studies, *J. Mar. Syst.*, 6, 109–119.
Ponte, R.M. (1993) Variability in a homogeneous global ocean forced by barometric pressure, *Dyn. Atmos. Oceans.*, 18, 209–234.

Price, J.F. (1979) On the scaling of stress driven entrainment experiments, *J. Fluid Mech.*, 90, 509–529.

Reason, C.J.C. and Power, S.B. (1994) The influence of the Bering Strait on the circulation in a coarse resolution global ocean model, *Clim. Dyn.*, 9, 363–369.

Reynolds, O. (1883) An experimental investigation of the circumstances which determine whether the motion of water shall be direct or sinuous, and of the law of resistance in parallel channels, *Philos. Trans. R. Soc. London*, 174, 935–982.

Reynolds, O. (1894) On the dynamical theory of incompressible viscous fluids and the determination of the criterion, *Philos. Trans. R. Soc. London*, 186, 123–161.

Robinson, A.R. (1987) Predicting open ocean currents, fronts and eddies, *Three-Dimensional Models of Marine and Estuarine Dynamics* (J.C.J. Nihoul and B.M. Jamart, Editors), Elsevier, pp. 89–111.

Rodi, W. (1993, 3rd edition) *Turbulence Models and their Application in Hydraulics. A State-of-the-Art Review*, IAHR-AIRH Monograph, A.A. Balkema, 104 pp.

Sambrotto, R.N., Goering, J.J. and McRoy, C.P. (1984) Large yearly production of phytoplankton in the Western Bering Strait, *Science*, 225, 1147–1150.

Sarmiento, J.L. (1992) Biogeochemical ocean models, *Climate System Modeling* (K.E. Trenberth, Editor), Cambridge University Press, pp. 519–551.

Semtner, A.J. and Chervin, R.M. (1992) Ocean general circulation from a global eddy resolving model, *J. Geophys. Res.*, 97, 5493–5550.

Sielecki, A. (1968) An energy-conserving difference scheme for the storm surge equations, *Mon. Weather Rev.*, 96, 150–156.

Toggweiler, J.R., Dixon, K. and Bryan, K. (1989) Simulation of radiocarbon in a coarse-resolution world ocean model, 2. Distributions of bomb-produced carbon 14, *J. Geophys. Res.*, 94, 8243–8264.

Waleffe, F. (1985) *Modèle Mathématique 3D de la Mer de Bering*, Mémoire de Fin d'Etudes, Faculté des Sciences Appliquées, Université de Liège, 126 pp.

Walsh, J.J., McRoy, C.P., Coachman, L.K., Goering, J.J., Nihoul, J.C.J., Whitledge, T.E., Blackburn, T.H., Parker, P.L., Wirck, C.D., Shuert, P.G., Grebmeier, J.M., Springer, A.M., Tripp, R.B., Hansell, D.A., Djenidi, S., Deleersnijder, E., Henriksen, K., Lund, B.A., Andersen, P., Müller-Karger, F.E. and Dean, K. (1989) Carbon and nitrogen cycling within the Bering/Chukchi Seas: source regions for organic matter affecting AOU demands of the Arctic Ocean, *Progr. Oceanogr.*, 22, 279-361.

Williamson, D.L. (1979) Difference approximations for fluid flow on a sphere, *Numerical Methods Used in Atmospheric Models*, GARP Publications Series (no. 17, vol. 2), WMO-ICSU Joint Organizing Committee, pp. 51–120.

Wimbush, M. and Munk, W. (1971) The benthic boundary layer, *The Sea* (Vol. 4) (A.E. Maxwell, Editor), Wiley, pp. 731–758.

Zhang, R.H. and Endoh. M. (1992) A free-surface general circulation model for the tropical Pacific Ocean, *J. Geophys. Res.*, 97, 11237–11255.

**Acknowledgements.** The development of the World Ocean model presented here is carried out in the scope of the Impulse Programmes "Global Change" (GC/10/13) and "Information Technology" (IT/SC/20) of the Belgian Federal Office for Scientific, Technical and Cultural Affairs. The support of the following projects is also acknowledged: Convention d'Actions de Recherches Concertées with the Communauté Française de Belgique (No. 92/97-154), the European Environment Programme (EV5V-CT92-0123) and Digital Europe External Research Agreement "World Ocean Modelling with a 'Small' Parallel Computer " (Contract Number BE–011).